©2010

Hee Taek Yi

ALL RIGHTS RESERVED

Functional transport properties in complex transition metal oxides

by

Hee Taek Yi

A Dissertation submitted to the

Graduate School-New Brunswick

Rutgers, The State University of New Jersey

in partial fulfillment of the requirements

for the degree of

Doctor of Philosophy

Graduate Program in Electrical and Computer Engineering

written under the direction of

Professor Sang-Wook Cheong

and approved by

New Brunswick, New Jersey

October, 2010

ABSTRACT OF THE DISSERTATION

Functional transport properties in complex transition metal oxides

By Hee Taek Yi

Dissertation Director: Professor Sang-Wook Cheong

Transition oxide materials have a long and high-flying history due to their attractive properties. They are well-known today for magnets, high temperature superconductors as well as promising electronic materials. For example, BaTiO₃ and PbZrTiO₃ are famous piezoelectric materials that are used in Micro-electric-mechanical system devices and VO₂, a metal insulator transition material with a threshold temperature of 70 degrees is used to prevent over-heating of devices such as batteries. Herein, I address the newly investigated noble transport properties in (1) perovskite (La,Pr,Ca)MnO₃ as a cryogenic non-volatile random access memory by using the phase change between charge-ordered insulating state and ferromagnetic metallic state, (2) ferroelectric BiFeO₃: switchable photovoltaic effect by switching the poling direction of the sample. I also explored the newly investigated multiferroic property in transition metal compound $Ca_3Co_{2-x}Mn_xO_6$ as well as the giant magnetic coercivity change induced by co-operative freezing in $Ca_3Co_2O_6$.

Acknowledgements

First of all, I confess that the goodness and mercy of God has led me to be here. He is my good shepherd and I am well provided from him. I would like to express my deep and sincere gratitude to my advisor, Professor Sang-Wook Cheong, for his constructive and detailed comments, and for his important support throughout this work. Working with him has awakened me to become a physicist with solid concepts and background. I express special thanks to my committee members, Professor Paul Panayotatos, Professor Wei Jiang, and Professor Weida Wu, for their advice and detailed review during the preparation of this thesis. My appreciation also goes to Professor Valery Kiryukhin and Porfessor Seongshik Oh for useful discussions. I express my gratitude to former and current group members, Sabya Guha, Soon Yong Park, Yoichi Horibe, Seongsu Lee, Young Jae Choi, Chenglin Zhang, Taekjib Choi, Toshihiro Asada, Seung Chul Chae, Mehmet Ramazanoglu, Nara Lee, Andrew Hogan, Steven Roden, Zhen Qin, Daniel Kwok, Sean Fackler, Bing Li and Mathew Vannucci. Each one of them has assisted in making my research possible and has made me enjoy lab life.

Finally, I sincerely express my loving thanks to my parents, parents-in-law and brother for their great love, endless support and their pray for me. I owe my loving thanks to my lovely wife, Seihee Min, and my son, Hankyu. Without their encouragement and understanding, it would have been impossible for me to finish this work.

Dedication

To my God

from alpha to omega

To my parents

Bae Keun Yi and Myung-Ja Choi

for who I am today and endless support

To my brother

Hee Seok Yi

To my son

David Hankyu Yi

Last but not least, to my beloved wife

Seihee Min

for her sacrifice, patience and love

Table of Contents

Abstract of the Dissertationii
Acknowledgementsiii
Dedicationiv
I. Introduction on applications in transition metal oxides1
1. Transition metal oxides
2. Non-volatile Random Access Memory5
3. Photovoltaic effect in Ferroelectrics
4. Multiferroics11
5. References17
II. Reversible Colossal Resistance Switching in (La,Pr,Ca)MnO ₃ ; cryogenic
non-volatile memories19
1. Introduction20
2. Experimental Method22
3. Results and Discussion25
4. Conclusions
5. References
III. Switchable diode and photovoltaic effect in ferroelectric BiFeO ₃
1. Introduction
2. Experimental Method40
3. Results and Discussion
4. Conclusions60

	5. References
IV.	Multiferroicity in an 1 D ising chain magnet Ca ₃ CoMnO ₆ 64
	1. Introduction65
	2. Experimental Method67
	3. Results and Discussion68
	4. Conclusions77
	5. References79
V.	Giant magnetic coercivity change induced by co-operative freezing in
	Ca ₃ Co ₂ O ₆
	1. Introduction82
	2. Experimental Method83
	 2. Experimental Method
	3. Results and Discussion83
VI.	3. Results and Discussion

Chapter I

Introduction on applications in transition metal oxides

1. Transition metal oxides

In the past several decades, numerous transition metal oxides (TMO) containing transition elements have been intensively researched due to their fascinating properties in bulk and/or as thin films. Transition elements are atoms that have electrons in the d-orbital. These elements are located in the *d*-block (group 3 to 12) of the periodic table (FIG I. 1). Group 3 such as Yttrium and Scandium and group 12 are not usually considered transition elements since their compounds contain no *d*-electron in group 3 (Se^{3+} : $3d^04s^0$) and completely-filled d-orbital in group 12 (Zn^{2+} : $3d^{10}4s^0$). Intriguing magnetic and electric properties of transition metal oxides are originated from the incompleted *d*-orbital electrons. For example, magnetic properties came from unpaired *d*-orbital electrons; atoms have odd numbers of *d*-electrons and/or even numbers of *d*-electrons in high spin and low spin state.

Applications of transition oxide materials, such as superconductivity and magnetoresistance effect, are well known. Low-loss power delivery/superconductivity is the most familiar application in transition metal oxide. Georg Bednorz and Karl Müller were jointly awarded the Nobel Prize in Physics in 1987 for their observation of high temperature superconductivity with cuprate (Ba-La-Cu-O system) ceramic materials. It laid the ground work that lead to the discovery of YBa₂Cu₃O₇, its critical temperature is above liquid nitrogen temperature [1,2]. The research on high temperature superconductor is recently intensified by the discovery of Fe-based superconductors in iron pnictide compounds. Modulation of electrical resistance in the presence of magnetic field (colossal and/or giant magnetoresistance in manganites) is also a famous property of transition oxide materials [3,4]. Electrical resistance can be decreased in the presence of a

1 A																		8 A
hydrogen 1 H	2A												3A	4 A	5A	6A	7A	^{bellum} 2 He
1.0079 lithium 3	beryllium 4	1										1	boron 5	carbon 6	nitrogen 7	oxygen 8	fluorine 9	4.0026 neon 10
Li 6.941	Be 9.0122												B 10.811	12.011	N 14.007	0 15.999	F 18.998	Ne 20.190
sodium 11	magnesium 12											Cast of the	aluminium 13	silicon 14	phosphorus 15	sulfur 16	chiorine 17	argon 18
Na 22,990	Mg 24.305	3	3B	4B	5 B	6 B	7B		8-		1B	2B	AI	Si 28.086	P 30.974	S 32.065	CI 35.453	Ar 39,948
potassium 19	calcium 20		scandium 21	titanium 22	vanadum 23	chromium 24	manganese 25	1000 26	cobalt 27	nickel 28	copper 29	zinc 30	gallium 31	germanium 32	arsenic 33	selenium 34	bromine 35	krypton 36
κ	Ca		Sc	Ti	۷	Cr	Mn	Fe	Co	Ni	Cu	Zn	Ga	Ge	As	Se	Br	Kr
39.098 rubidium 37	40:078 strontium 38		44.966 yttrium 39	47.867 zirconium 40	50.942 niobium 41	51.996 molybdenum 42	54.938 technetium 43	55.845 ruthenium 44	58.933 rhodium 45	58.693 palladium 46	63.546 silver 47	65.39 cadmium 48	69.723 indium 49	72.61 tin 50	74.922 antimony 51	78.96 tellurium 52	79.904 kodine 53	83.80 xenon 54
Rb	Sr		Y	Zr	Nb	Mo	Tc	Ru	Rh	Pd	Ag	Cd	In	Sn	Sb	Те	1	Xe
85.468 caesium 55	87.62 barlum 56	57-70	88.906 lutetium 71	91.224 hatnium 72	92.906 tantalum 73	95.94 tungsten 74	[98] rhenium 75	101.07 osmium 76	102.91 Iridium 77	106.42 platicum 78	107.87 gold 79	112.41 mercury 80	114.82 thallium 81	118.71 lead 82	121.76 bismuth 83	127.60 polonium 84	126.90 astatine 85	131.29 radon 86
Cs	Ba	*	Lu	Hf	Та	W	Re	Os	Ir	Pt	Au	Hg	TI	Pb	Bi	Po	At	Rn
132,91 francium 87	137.33 radium 88	89-102	174.97 lawrencium 103	178.49 rutherfordium 104	180.95 dubnium 105	183.84 seaborgium 106	186.21 bohrium 107	190.23 hassium 108	192.22 meitnerkum 109	195.08 ununnillum 110	196.97 unununium 111	200,59 ununbium 112	204.38	207.2 ununguadium 114	208.98	209	[210]	[222]
Fr	Ra	* *	Lr	Rf	Db	Sg	Bh	Hs	Mt	Uun	Uuu	Uub		Uuq				
[223]	[226]		[262]	[261]	[262]	1266	[264]	[269]	[268]	[274]	[272]	[277]		[289]	1			

anthanum 57	cerium 58	praseodymium 59	neodymkum 60	promethium 61	samarium 62	europium 63	gadolinium 64	terbium 65	dysprosium 66	holmium 67	erbium 68	thulium 69	ytterbium 70
La	Ce	Pr	Nd	Pm	Sm	Eu	Gd	Tb	Dy	Ho	Er	Tm	Yb
actinium 89 AC	90 Th 232.04	protactinium 91 Pa 231.04	uranium 92 U 238.03	neptunium 93 Np	patonium 94 Pu 12441	americium 95 Am	curium 96	97 Bk	californium 98 Cf	einsteinium 99 ES	100 Fermium 100 Fm	mendelevium 101	nobelium 102 No

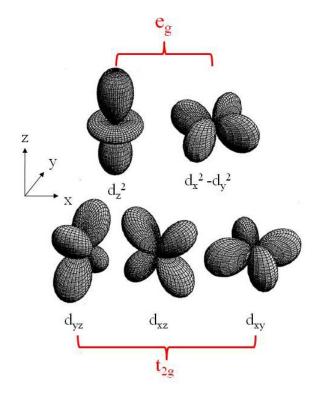


FIG. I. 1. Periodic table and angular distribution of the d orbital

magnetic field. This observation of the magnetoresistance effect earned Albert Fert and Peter Grünberg a Nobel Prize in Physics in 2007. The Magnetoresistance effect offers an opportunity for the development of new technologies such as read/write heads for ultra high-capacity magnetic storage and spintronics. The examples of applications in TMO materials are shown in FIG. I. 2.

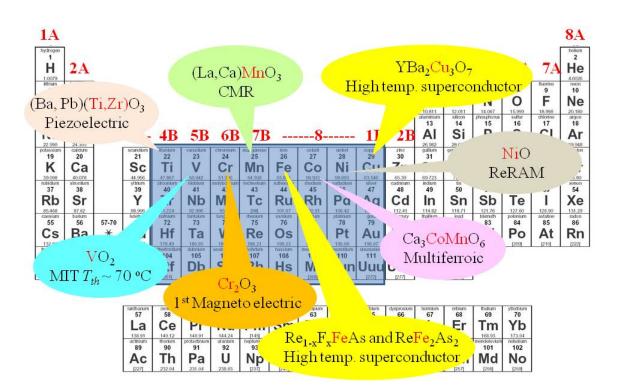


FIG. I. 2. Examples of transition metal oxide application

2. Non-volatile Random Access Memory

Non-volatile Random Access Memory (RAM) is defined as memory device that does not lose its storage information when the power is turned off. This non-volatile RAM effect has been observed in a wide variety of transition metal oxide, such as Pr_{0.7}Ca_{0.3}MnO₃, Cr-doped SrZnO₃, and SrTiO₃ [5-7]. The trend of recent technology is that devices are becoming more compact and some are even conversed into a multifunctional device, such as a smart phone. The non-volatile RAM is an essential device for recent technologies. Non-volatile memory is required to have speed of a static RAM, and storage density of a dynamic RAM. Flash memory used as a non-volatile memory but there is a limit of speed (FIG I. 3).

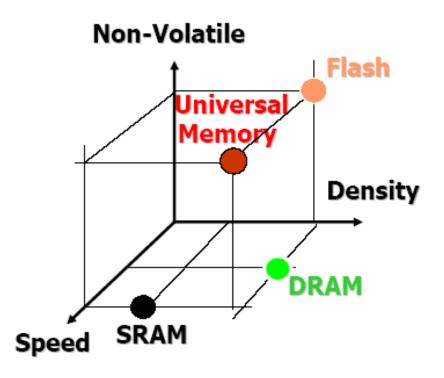


FIG. I. 3. Schematic of relation among memory devices

For this reason, new concepts of RAM have been researched and parts of them are developed as a product such as Ferroelectric RAM, which uses a ferroelectric property and Magenetoresistive RAM, which utilizes magnetoresistivity. Recently, reversible resistance switching effect (the resistance of the device can be reversibly switched by applied electric pulses) is observed in Pr_{0.7}Ca_{0.3}MnO₃ and has drawn attracted much attention as it is a good candidate for non-volatile Resistance-RAM [8,9]. This resistivity switching in Resistance-RAM (R-RAM) turns out to be caused by formation and annihilation of nanoscale conducting paths. The microscopic mechanism of the R-RAM effect is not fully understood yet, but is theorized to be associated with the local phase change with different electronic properties, similar to how Phase change RAM (P-RAM) works [10,11].

In R-RAM case, high resistance state and low resistance state are changed by creation and annihilation of filament path. As applied voltage increase, conduction paths like filament, develop throughout the sample. The memory device then becomes a low resistance state. And at low resistance state, increasing the applied voltage, the conduction path is broken and becomes a high resistance state (FIG. I. 4). The mechanism of Phase change RAM is shown in FIG. I. 5. The P-RAM shows a high resistance and low reflectance behavior in the amorphous form (reset state), while the crystalline phase (on state) shows a low resistance and high reflectance. These "reset" and "on" states can be switched from one to the other by using different voltage or laser pulses that induce either heating above the melting temperature followed by rapid quenching or annealing below the melting temperature but above the glass transition temperature. The P-RAM provides high sensing margins. Both P-RAM and R-RAM have

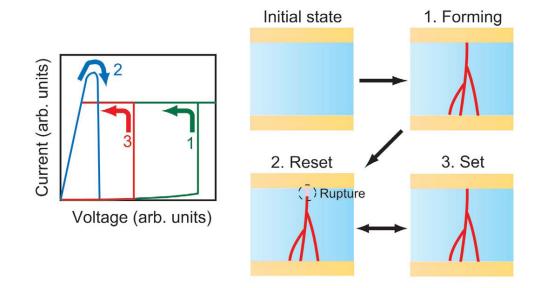


FIG. I. 4. Mechanism of the R-RAM and I-V character in STO and PCMO [material Tod]

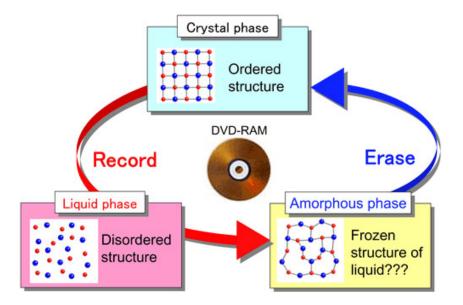


FIG. I. 5. Mechanism of the P-RAM [12]

attracted a great deal of attention for use as future nonvolatile memories. In Chapter II, I shall address the newly investigated novel transport properties in perovskite (La,Pr,Ca)MnO₃ as a cryogenic non-volatile random access memory by using phase change between charge-ordered insulating state and ferromagnetic metallic state.

3. Photovoltaic effect in Ferroelectrics

Conventional photovoltaic effect in non-polar materials is well-known photovoltaic effect in p-n junction. This effect originates from the internal field in the space charge region. The homogeneous illumination of light, which its energy is larger than the material's bandgap, generates electron-hole pairs in the specimen. Generated electron-hole pairs in the space charge region move in a one direction under the internal field which is induced by band bending in the junction. The main drawback of p-n junction solar cell lies in the high temperature fabrication techniques used to build carrier difference in bulk and grain boundary diffusion of the dopant in polycrystalline material.

In 1956, Bell laboratory scientist A. G. Chynoweth reported steady photovoltaic current in BaTiO3 [13]. He explained that the ferroelectric photovoltaic effect (FPV) was related with the internal fields induced space charge region. In 1986, Dr. Gower measured ~1 nA on/off photocurrent in BaTiO₃ by using a multimode Ar laser at 488 nm. In 1972, Japanese scientist reported the FPV effect in ferroelectric TiO₂ and another Bell laboratory scientist Dr. Glass's bulk photovoltaic effect in LiNbO3 published in 1974. Ferroelectric materials have a spontaneous electric polarization which came from space inversion symmetry breaking in different directions. Polarization can be reversely changed by application of an external electric field larger than electric coercivity of that

material. In ferroelectrics, structural instability caused by the change in chemical bonding is a primary driver for ferroelectricity. Such materials mostly have been found in transition metal oxides that have perovskite structure, ABO₃, as shown in FIG. I. 6. The cations in A and B sites occupy the corners in the cubic unit cell, and at the center of the octahedron formed by oxygen anions. BaTiO₃ has Ti⁴⁺ ions in the B site with no electrons in the 3*d* shell, so they tend to form strong covalent bonds with neighboring O²⁻ ions.

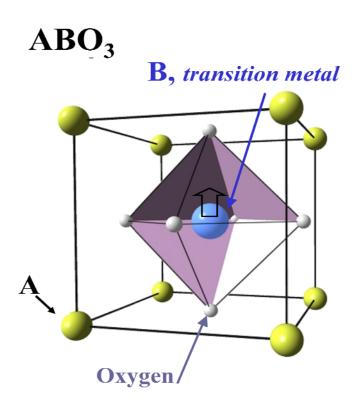


FIG. I. 6. The large cation in A site (yellow balls) occupy the corners in the unit cell. The small cation in B site (a blue ball) lies at the center of an octahedron formed by oxygen anions (silver balls). For YMnO₃, the Yttrium and Manganese occupy A site and B site respectively.

The presence of non-zero d electrons in ferroelectrics with transition metals can result in large cross-coupling effects between magnetism and ferroelectricity in multiferroics [14-18]. These effects have drawn enormous attention, especially in fields integrating new technologies such as multi-level memory devices [16-18] or inexpensive and highly-sensitive magnetic sensors. Ferroelectrics are materials that have ferroelectric domains with space inversion symmetry broken in different directions that can be switched with an external electric field [19]. They are often highly insulating and associated with large band gaps [20]. Thus, little investigation of DC transport properties in single ferroelectric domains has been performed. On the other hand, photocurrents can be induced by high-energy (often UV range) light illumination, and associated photovoltaic effects have been studied in ferroelectrics [21-25]. When a ferroelectric in an open circuit is illuminated by UV light, a high photovoltage, much larger than the band gap, can develop in the direction of electric polarization. The magnitude of this photovoltage is directly proportional to the crystal length in the polarization direction. In addition, a steady-state photovoltaic current can be generated in the direction of electric polarization when a ferroelectric, under continuous light illumination, forms a closed circuit. This photovoltaic effect of ferroelectrics, distinctly different from the typical photovoltaic effect in semiconductor p-n junctions, is investigated for, e.g., Pb-based ferroelectric oxides [21-23] and LiNbO₃ [24, 25]. This photovoltaic current turns out to be minuscule – on the order of pico-to-nano-Amperes [22,23,25]. Evidently, utilization of small charge-gap ferroelectrics with good carrier transport properties and large absorption of visible light extending into the red range is of fundamental importance for practical applications in increasing power conversion efficiency and thereby harvesting more solar

energy. In Chapter III, I shall address the investigated novel switchable photovoltaic effect in Ferroelectric BiFeO₃.

4. Multiferroics

Magnetism and ferroelectricity are widely applied to many forms of recent technology. Magnetic information can be written/erased by applying a magnetic field in ferromagnetic materials, and electric polarization can be tuned by applying an electric field in ferroelectric materials. If cross-coupling between magnetism and motion of electric charges, which Maxwell's equations predicted, is realized, it might be great help for tuneable multifunctional devices. For this reason, the number of reported research papers has been increased exponentially since 2000 as shown in Fig. I. 7 and over 350 papers have been published only in 2009.

Useful applications by using ME effect have not yet been realized in a single material due to the general weakness of the ME effect. The ME effect device can be strengthened by stacking piezoelectric and magnetostrictive materials such as $PbZr_{1-x}Ti_xO_3(PZT)$ and $Tb_xDy_{1-x}Fe_2$ alloy (Terfenol-D) respectively as shown in Fig. I. 8. By applying the magnetic field in the stacked sample, the Terfenol-D material undergoes mechanical change, changing of shape and/or dimensions and that length change induces the strain stress in piezoelectric material, which generates electricity.

Why are there so few ME materials, which have both ferroelectric and magnetic behavior so called multiferroic? Dr. Hill went into detail about that question in his article [28]. First, ferromagnetic materials show often metallic behavior. Fe, Ni, Co and their alloys have high density of states at the Fermi level. This high density of states results in

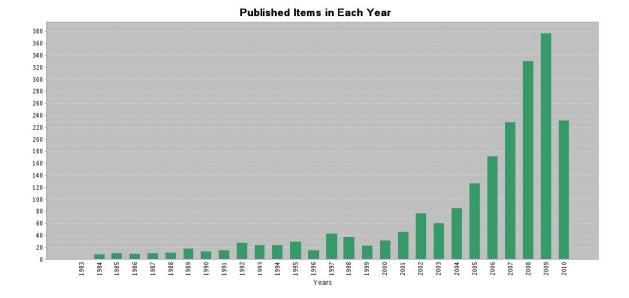


FIG. I. 7. Publications per year searched with a keyword of "magnetoelectric" according to the Web of science [26].

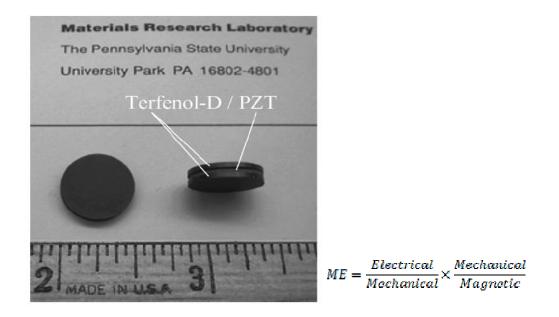


FIG. I. 8. Laminated sample, a PZT/Terfenol-D trilayer disc and the mechanism of stacking ME effect [27].

metallic behavior. On the contrary, ferroelectric materials show insulating behavior, if not, large leakage current prevents formation of electrical polarization in these materials. Note that ferrimagnets and weak ferromagnets are usually insulating materials. Second, magnetic properties came from unpaired *d* shell electrons of transition metal ions like Fe, Ni, and Co. While most ferroelectrics have empty d state of transition metal oxides which tend to hybridize with oxide 2p ions.

The presence of non-zero d electrons in ferroelectrics containing transition metals can result in large cross-coupling effects between magnetism and ferroelectricity in multiferroics [18, 29-32]. Dr. Cheong and Dr. Mostovoy report a conceptually important model in which a collinear spin order induces ferroelectricity through symmetric superexchange [33]. As illustrated in FIG. I. 9(a), up-up-down-down ($\uparrow \downarrow \downarrow \downarrow$)-type spin order can be constructed using an Ising spin chain with competing nearest-neighbor ferromagnetic (J_F) and next-nearest-neighbor antiferromagnetic (J_{AF}) interactions ($|J_{AF}/J_F|>1/2$). If the charges of magnetic ions alternate along the chain, this magnetic ordering breaks inversion symmetry on magnetic sites. Favoring ferromagnetic nearestneighbor spin coupling, ions are shifted away from their centro-symmetric positions (dotted red circles), inducing electric polarization via exchange striction along the chain direction.

The diagram in Fig. I. 10 schematically shows why the alternations with different valences are required for magnetism induced ferroelectricity. For $|J_{AF}/J_{F}|>1/2$, $\uparrow\uparrow\downarrow\downarrow$ spinorder can be stabilized. Afterwards, ferromagnetic spins attract each other while the antiferromagnetic spins repel each other. To check whether space inversion symmetry is broken or not, we can take the space inversion operation by moving the spin on the right

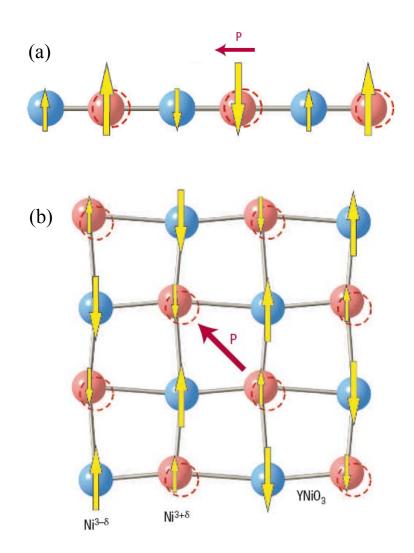


FIG. I. 9. (a) Polarization induced by exchange striction of alternating magnetic ions having up-up-down-down spin order. (b) Possible polarization along the diagonal direction in the *ab* plane of YNiO₃. [33]

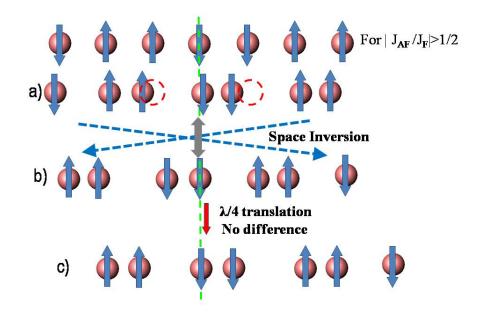


FIG. I. 10. (a) up-up-down-down spin order same magnetic ions and shift of ions by Inverse goodenough Kanamori rule (b) ionic order after space inversion operator (c) $\lambda/4$ translated ionic order

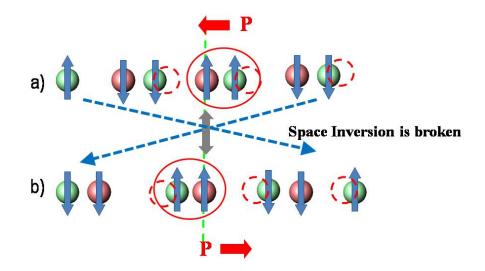


FIG. I. 11. (a) up-up-down-down spin order with same magnetic ions and shift of ions (b) ionic order after space inversion operator (c) ionic order after $\lambda/4$ translation

side to the left, and left one to the right. The green dotted line indicates inversion center. By doing this space inversion operation for Fig. I. 10 (a), you can have the arrangement of (b). Figure (b) may look differ from (a). But we translate it $\lambda/4$, that one is same with (a). We can not distinguish them. This spin order itself doesn't break the inversion symmetry.

If we have different ions with alternating fashion, then ferroelectric polarization can be induced along the chain direction and a charge ordering like alternating in two different charges, red-green-red-green appears. Then this whole arrangement can break inversion symmetry and induce ferroelectric polarization along the chain direction as shown in Fig. I. 11 (a). By doing space inversion operation for (a), the arrangement of (b) is established. Fig. I. 11 (b) cannot be overlapped with (a) by doing any translational movement. Inversion symmetry is broken in this arrangement. There are two types of magnetic clusters depending on the arrangement and they have opposite signs of polarization. This theoretical prediction has been remarkably realized in an Ising chain magnet of $Ca_3(Co,Mn)O_6$ and more details will be discussed in Chapter IV. Another type of application in giant magnetic coercivity change induced by co-operative freezing in $Ca_3Co_2O_6$ shall be discussed in Chapter V.

2. References

[1] N. N. Greenwood, and A. Earnshaw, *Chemistry of the elements*. Butterworth-Heinemann, (1997)

[2] K. M. Wu, J. R. Ashburn, C. J. Torng, P. H. Hor, L. Meng, L. Gao, Z. J. Huang, Y.Q. Wang, and C. W. Chu, Phys. Rev. Lett. **58**, 908 (1987).

[3] R. von Helmolt, J. Wecker, B. Holzapfel, L. Schultz, and K. Samwer, Phys. Rev. Lett. **71**, 2331 (1993).

[4] A. P. Ramirez, J. Phys.: Condens. Matter 9, 8171 (1997).

[5] S.Q. Liu, N. J. Wu, and A. Ignatiev, Appl. Phys. Lett. 76, 2749 (2000).

[6] A. Beck, J. G. Bednorz, Ch. Gerber, C. Rossel, and D. Widmer, Appl. Phys. Lett. 77, 139 (2000).

[7] Y. Watanabe, J. G. Bednorz, A. Bietsch, Ch. Gerber, D. Widmer, A. Beck, and S. J. Wind, Appl. Phys. Lett. **78**, 3738 (2001).

[8] K. Szot, W. Speier, G. Bihlmayer, and R. Waser, Nature Mater. 5, 312 (2006).

[9] R. Waser, and M. Aono, Nature Mater. 6, 833 (2007).

[10] S. R. Ovshinsky, Phys. Rev. Lett. 21, 1450 (1968).

[11] J. Hegedűs, and S. R. Elliott, Nature Mater. 7, 399 (2008).

[12] See for example: lightsources, http://www.lightsources.org/cms/?pid=1001659

[13] A. G. Chynoweth, Phys. Rev. 102, 705 (1956).

[14] N. A. Hill, J. Phys. Chem. B 104, 6694 (2000).

[15] H. Schmid, Ferroelectrics 162, 317 (1994).

[16] T. Kimura, T. Goto, H. Shintani, K. Ishizaka, T. Arima, and Y. Tokura, Nature **426**, 55 (2003).

[17] N. Hur, S. Park, P. A. Sharma, J. S. Ahn, S. Guha, and S.-W. Cheong, Nature **429**, 392 (2004).

[18] Y. Yamasaki, S. Miyasaka, Y. kaneko, J.-P. He, T. Arima, and Y. Tokura, Phys. Rev. Lett. **96**, 207204 (2006).

[19] J. F. Scott, Ferroelectric Memories (Springer, Heidelberg, 2000).

[20] M. Dawber, K. M. Rabe, J. F. Scott, Rev. Mod. Phys. 77, 1083 (2005).

[21] M. Qin, K. Yao, Y. C. Liang, S. Shannigrahi, J. Appl. Phys. 101, 014104 (2007).

[22] P. Poosanaas, A. Dogan, S. Thakoor, K. Uchino, J. Appl. Phys. 84, 1508 (1998).

[23] L. Pintilie, I. Vrejoiu, G. L. Rhun, M. Alexe, J. Appl. Phys. 101, 064109 (2007).

[24] A. M. Glass, D. Von der Linde, T. J. Negran, Appl. Phys. Lett. 25, 233 (1974).

[25] G. Dalba, Y. Soldo, F. Rocca, V. M. Fridkin, Ph. Sainctavit, Phys. Rev. Lett. 74, 988 (1995).

[26] See for example: Web of Science, http://apps.isiknowledge.com/CitationReport

[27] Ryu J, Carazo A V, Uchino K, and Kim H E, J. J. Appl. Phys. 40, 4948 (2001)

[28] Nicola A. Hill, J. Phys. Chem. B 104, 6694 (2000)

[29] T. Kimura, J. C. Lashley, and A. P. Ramirez, Phys. Rev. B 73, 220401(R) (2006).

[30] S. Seki, Y. Onose, and Y. Tokura, Phys. Rev. Lett. 101, 067204 (2008).

[31] K. Taniguchi, N. Abe, T. Takenobu, Y. Iwasa, and T. Arima, Phys. Rev. Lett. 97, 097203 (2006).

[32] T. Kimura, G. Lawes, and A. P. Ramirez, Phys. Rev. Lett. 94, 137201 (2005).

[33] S-W. Cheong and M. Mostovoy, Nature Mater. 6, 13 (2007).

Chapter II

Reversible Colossal Resistance Switching in (La,Pr,Ca)MnO₃; cryogenic non-volatile memories

1. Introduction

Cryogenic-temperature electronics technologies are a practical promise for continuing demand for high performance electronics such as many types of quantum computers [1-4], Superconducting Rapid Single Flux Quantum (RSFQ) devices [5-7], and cryogenic detectors [8-10]. One of the critical bottle necks for cryo-electronics is low-temperature memories. For example, the RSFQ devices can have up-to-800 GHz circuit speed at 4 K, and thus is the most promising technology in the continuing demand for faster processors [7]. However, the key area of risk for the RSFQ technology has been identified as low-temperature (T) memories [7]. Furthermore, many types of quantum computers, based on completely new processing concepts of quantum superposition and entanglement, operate at very low temperatures, and future electronics with these quantum computers will eventually require low-T memories. In addition, the sensitivity of a number of detectors such as modern CCD (charge-coupled device) cameras can be greatly enhanced at low temperatures, and cryogenic memories can be facilitated in new electronics with low-T detectors. Proposed candidates for the cryogenic memories include CMOS-based RAM (similar with flash memory) and Magnetoresistive RAM (M-RAM, using magnetic tunneling junctions) [11]. However, few experiments have been reported for low-T memory devices. Evidently, new device concepts for the cryogenic memories are in great demand. Herein, by utilizing the unique hysteretic behavior of perovskite (La,Pr,Ca)MnO₃ in the variation of temperature and applied electric fields, we have discovered 1) low-temperature phases with metallic and insulating resistance values (different by $>10^5$) can be repeatedly switched by applying various voltage pulses, 2) the resistance value of each phase is highly repeatable through cycling and also stable with

time, and 3) intermediate phases with intermediate resistance values can be also repeatedly stabilized. Harnessing these unprecedented behaviors can enable cryogenictemperature phase-change random access memory (cryoP-RAM) applications, compatible with, e.g., the RSFQ technology.

Change of physical phases at room temperature with applied voltage or laser pulses has been exploited for non-volatile memories such as P-RAM, DVD-RW (Read/Write) or Resistance-RAM (R-RAM) [12-16]. Chalcogenides such as Ge₂Sb₂Te₅ have been utilized for P-RAM and DVD-RW. Chalcogenides in the amorphous form (reset state) exhibit high resistance and low reflectance while the crystalline phase (on state) shows low resistance and high reflectance. The states can be switched by using different voltage or laser pulses that induce either heating above the melting temperature followed by rapid quenching or annealing below the melting temperature but above the glass transition temperature. The ratio between low and high resistances can be greater than 1000, which provides high sensing margins. Resistivity switching with applied voltage pulses can occur repeatedly in many transition metal oxides, which is the base R-RAM. The resistivity switching turns out to be due to formation and annihilation of nanoscale conducting paths. The microscopic mechanism of the R-RAM effect is not fully understood yet, but is associated with the filamentary phase change with different electronic properties, somewhat similar to how P-RAM works. Both P-RAM and R-RAM have attracted a great deal of attention for use as next-generation nonvolatile memories at room temperature (T).

Hysteretic behaviors of collective electronic phase transitions with external perturbations can accompany memory effects with, for example, the large change of

resistance and fast response time. It has been well established that doped perovskite manganites tend to have colossal response to external perturbations such as applied magnetic fields, electric fields, external pressure, x-ray or visible-light illumination or electron beams [17-24]. The effect is particularly large in systems that locate near the bicritical point between ferromagnetic-metallic (FM) and charge-ordered-insulating (COI) states, such as Pr_{0.7}Ca_{0.3}MnO₃ (PCMO) or (La_{1-x-y}Pr_xCa_y)MnO₃ (LPCMO) with x and y near 3/8. For example, when a gradually-increasing voltage on PCMO reaches the threshold value, resistance drops by three orders of magnitude at low T, indicating a transition from insulating to metallic phases. However, the insulating phase returns when applied voltage is reduced to low values or zero [19,20]. Reproducibility and temporal stability of the above effect have not been investigated. In addition, it has not been established that the induced metallic phase can be switched back to the insulating phase by applying voltages, which is necessary for nonvolatile memory applications. If the transition between insulating and metallic phases in LPCMO is repeatedly switchable, then it can be utilized for a low-T analogue of P-RAM or R-RAM – cryoP-RAM.

2. Experimental Method

 $La_{0.25}Pr_{0.375}Ca_{0.375}MnO_3$ single crystals were grown using a floating zone furnace. A solid-state reaction method in air was employed to prepare feed rods for the floating zone growth. The schematic draw of our floating zone machine and floating zone sample are shown in FIG. II. 1. A 2x2x1 mm3-size specimen was prepared by cutting and polishing the grown crystal, and the surfaces of the crystal specimen were cleaned with dilute nitric acid and dilute bromine. A gold paint was used for 150 µm-diameter

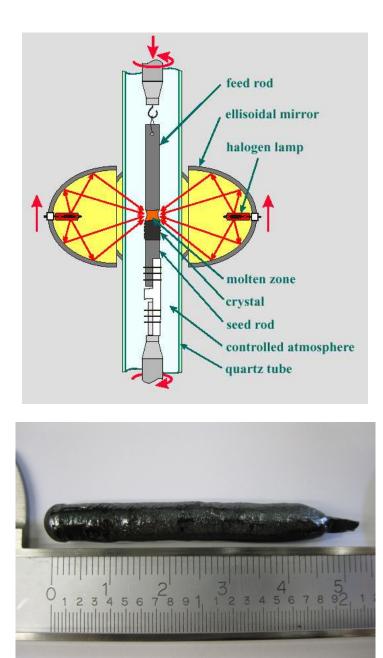


FIG. II. 1. The schematic of floating zone method and a single crystal made by floating zone method.

electrodes, and 2 mil gold wires were used for electric leads as shown in FIG. II. 2.

The distance between two-probe electrodes was ~100 μ m. The specimen was annealed at 1173 K for 1 hour in an oxygen atmosphere in order to remove strain during polishing and also to cure Au contacts. The temperature of the specimen during experiments was controlled by the Quantum Design PPMS, and the current-voltage measurements were performed with a Keithley 2400. The current noise of ~10⁻¹¹ A originates from the resolution limit of Keithley 2400.

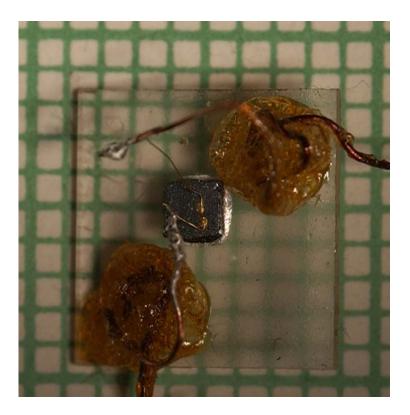


FIG. II. 2. The figure of sample contact.

3. Results and Discussion

The *T*-dependent four-probe resistivity of LPCMO with $Pr_{0.41}$ in various magnetic fields (*H*) is shown in FIG. II. 3(a) [26]. Red and blue arrows depict the routes for insulator-to-metal and metal-to-insulator changes, respectively. The huge change of resistivity with applied *H* reflects the essence of colossal magnetoresistance effect. The strategy we have taken to achieve a cryoP-RAM effect is as follows: the insulating phase in zero or very-low voltages at low *T* may be switched to a metallic phase (red color arrow in FIG. II. 3(a) when an appropriate voltage pulse is applied. When a large voltage pulse is applied to the induced metallic phase, a large current can be generated in the metallic region and consequently significant heating can occur. When a sufficient voltage is applied, the LPCMO can be heated to the high-*T* insulating phase. When the LPCMO is quickly cooled down to a low *T* from the high *T*, the insulating phase may remain. The transition from metallic to insulating phases may follow the blue color arrow in Figure 1(a). In order to implement the above strategy, we performed two-probe resistance (*R*) experiments on the set-up depicted in the inset of FIG. II. 3(b).

The *T*-dependence of two-probe *R* in various applied DC voltages (3 V, 5 V, 6 V, 9 V, and 10 V) is shown in FIG. II. 3(b). The temperatures at which resistance changes abruptly upon cooling and warming were defined as $T_c^{\ c}(V)$ and $T_c^{\ w}(V)$, respectively. Filled circles represent the data for the cooling measurement, while empty circles are taken upon warming after cooling in the presence of applied electric fields (FCW). The schematic of the specimen for our two-probe measurement is shown in the inset. With decreasing *T* in the presence of a voltage (*V*), *R* gradually increases until a critical *T* ($T_c^{\ c}(V)$) is reached, and then drops precipitously below $T_c^{\ c}(V)$. When *T* is varied below

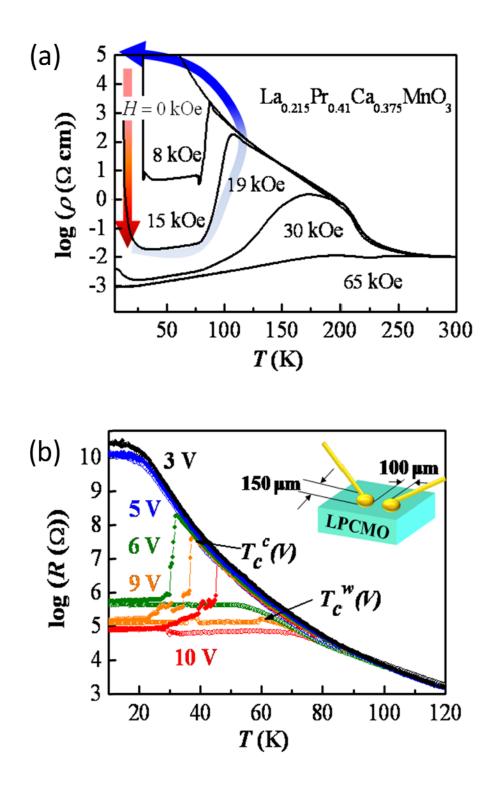


FIG. II. 3 (a) four-probe resistivity in various magnetic fields. (b) two-probe resistance with various voltages.

~25 K, *R* in a fixed *V* does not change within our experimental uncertainty, i.e. the *R* locks in below ~25 K. For low voltages (≤ 5 V), no hint of the presence of $T_c^c(V)$ was observed down to 2 K. The conducting state below $T_c^c(V)$ remains intact upon warming until *T* reaches $T_c^w(V)$, where *R* resumes the behavior of the high-*T* state. Most of these remarkable *R* behaviors have been understood in term of the coexistence of FM and COI phases whose volume fractions change with *T* and *V*. For example, the insulating behavior of the low-*T* phase in low *V* indicates that the phase is in a mostly COI state. The precipitous drop of *R* in high *V* at $T_c^c(V)$ stems from the formation of percolative conducting paths through FM regions in the presence of COI matrix [17,25,26].

The lock-in of the *R* value below ~25 K is due to cooperative freezing of phaseseparated FM and COI regions corresponding to simultaneous freezing of spin/charge/lattice degrees of freedom – which we will call a multiple-glass (MG) transition [26,27].

I(V) curves at various *T* are shown in FIG. II. 4(a) demonstrate 1) the red-arrow step in Fig.1 is readily achievable and 2) the isothermal threshold voltage from insulating to metallic phase depends significantly on temperature. The voltage for a step-like increase of current at a fixed *T* corresponds to the threshold voltage ($V_{th}(T)$) at the *T* (plotted in FIG. II. 4(b)), and there exists a strong *T* dependence of $V_{th}(T)$ below $T \leq 55$ K, but no significant step-like feature in I(V) was observed above 55 K. When a metallic phase is induced by voltages above $V_{th}(T)$, the metallic phase remains when that applied voltage is reduced to zero. Note that a virgin state is prepared for each measurement, i.e., the sample was heated up to 300 K and then cooled to a specific *T* without external field before measuring each I(V) curve. $T_c^c(V)$ and $T_c^w(V)$ from Fig. 1(b) are plotted in the *V*-*T*

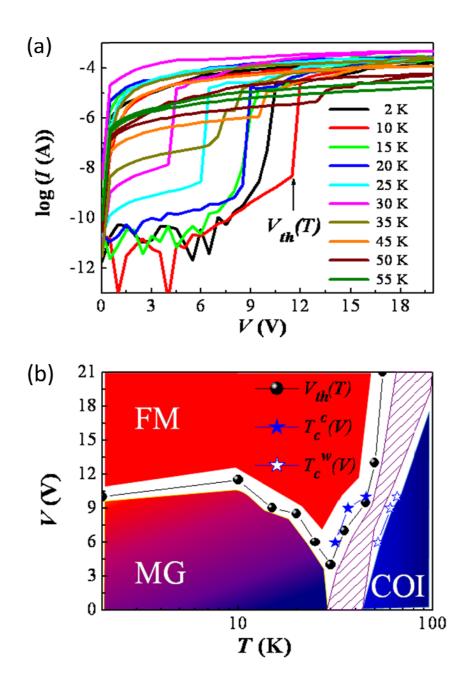


FIG. II. 4 (a) Logarithmic current versus applied voltage characteristics at various temperatures. $V_{th}(T)$ is defined as the isothermal threshold voltage. (b) Voltage versus logarithmic temperature plot. This schematic phase diagram is constructed from the results in FIG. II. 3(b) and FIG. II. 4(a). Area marked with black hatched lines represents the hysteretic FM/COI phase boundary.

diagram, and $T_c^c(V)$ points nicely match with $V_{th}(T)$ data. $V_{th}(T)$ shows a clear dip at ~30 K, slightly above the MG transition $T(T_{MG})$ of ~25 K. Strong dynamic phase fluctuations just above T_{MG} are probably responsible for the significant reduction of $V_{th}(T)$ at ~30 K.

We discovered that the metallic phase induced by a single voltage pulse of ~10 V (1 ms; tested limit) returns back to the insulating phase when a single large- voltage somewhat different from the virgin insulating state. FIG. II. 5 and FIG. II. 6 show the 2 K I(V) curves of differently-prepared phases. The black points in FIG. II. 6 represent the virgin insulating phase. A metallic phase is induced when applied voltage exceeds $V_{th}\approx10$ V at 2 K, and it remains metallic even when voltage is removed or negative small voltages are applied (FIG. II. 5.). Applying a single 65 V (~56 mW) pulse returns the metallic phase to an insulating phase (dark blue points in FIGs. 3(a) and the bottom three data sets in FIG. II. 6)

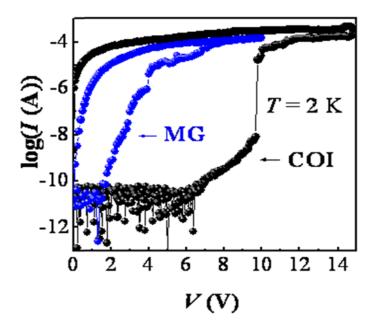


FIG. II. 5. Log (I(A)) versus V(V) characteristics of charge-ordered insulating (virgin insulating) and multiple-glass (induced insulating) phases at 2K.

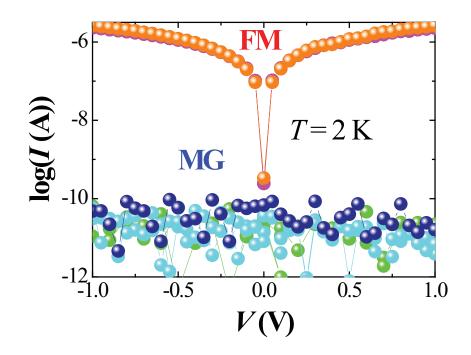


FIG. II. 6. Log(I)-V curves of multiple-glass and ferromagnetic-metallic phases at 2K. The curves are obtained on six consecutive states (alternating between induced insulating and metallic phases), and three sets of curves for each phase coincide with each other well, confirming high reproducibility.

However, the threshold voltage of this insulating phase for the insulator-to-metal transformation is only ~ 2 V. Therefore, the induced insulating phase appears distinct from the virgin insulating phase. Note that the virgin insulating phase was prepared by heating up to 300 K and then cooling back to 2 K in zero voltage. In terms of insulator/metal phase separation, we can speculate the origin of the difference between the virgin insulating and induced insulating phases. The virgin insulating phase may be in a MG state with mostly the COI phase.

It is established that the transformation of the virgin insulating to metallic phase is an electric field effect, rather than a Joule heating effect. In fact, the \sim 70 nW-power effect of the single 10 V pulse should be minimal. However, the Joule heating by the single 65 V (~56 mW) pulse on ~100 μ m–size metallic sample can be significant, so the sample with a 65 V pulse may experience the thermal cycling outlined with the blue curve in Fig. 1(a).

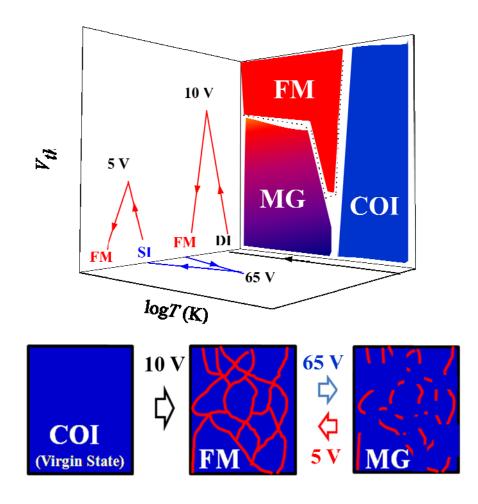


FIG. II. 7. Schematics of phase diagram and various phases; charge-ordered insulating (COI), multiple-glass (MG), and ferromagnetic-metallic (FM) phases. Red lines in the MG and FM cartoon represent the presence of FM metallic regions.

(65 V, 10 ms) pulse is applied. However, the induced insulating phase turns out to be

However, it is possible that a part of the initially-induced metallic regions may not be completely removed in tiny length scales during the thermal cycling, so the induced insulating phase after the thermal cycling may be in a MG state with a non-trivial amount of metallic regions, and may be more susceptible to the insulator-to-metal transformation by applied voltages. This scenario is schematically outlined in FIG. II. 7: for the sake of simplicity, we call the virgin insulating, induced metallic, and induced insulating phases as the COI, FM, and MG phases, respectively.

We would like to emphasize a few remarkable observations beneficial to memory applications. First, the observed resistance change is truly colossal - more than 5 orders of magnitude at, e.g., ± 1 V. Current signals for the insulating states are noisy and near 10^{-11} A, close to the current resolution limit of the Keithley 2400 used for our two-probe *R* measurement. The amount of 10^5 in resistance change is a lower bound. In addition, this transformation from induced insulating to metallic phases is highly reproducible and stable: three sets of *I(V)* curves for induced insulating or metallic phases in FIG. II. 6 are indistinguishable. This reproducibility and stability will be further discussed below. Finally, note that contrary to the huge Joule heating (from 300 K to ~600 °C) required for chalcogenide-based P-RAM, the required Joule heating for LPCMO should be significantly less, because of low specific heat values at low temperatures and also a small cycling temperature interval (~100 K).

We have further experimented the reproducibility and stability of the resistance switching, essential for memory applications. After applying a single 65 V pulse to form the MG phase ("off" resistance state), the current was measured for 300 s with 1 V reading voltage. Afterwards, currents were measured for another 300 s with 1 V reading

voltage right after a single 5 V (1 ms) pulse: the high current corresponds to the FM phase ("on" resistance state). The same cycle was repeated with different time duration (150 s, 60 s and 30 s) in a sequence. These results are summarized in FIG. II. 8(a). Blue and red circles indicate off and on resistance states, respectively. The voltage pulses of ~5 V and ~65 V were used to create the on and off states. Note that we found that there is no hint of degradation of resistance in each state in our overnight experiments. As shown in FIG. II. 8(b), the on/off ratio is $>10^5$, and maintains the same value over a number of switching cycles. The voltage sequence of 5 V (insulator-to-metal switching) -1 V (reading) - 65 V (metal-to-insulator switching) -1 V (reading) was used for each cycle, as schematically shown in the inset figure of the FIG. II. 8(b).

We also found that intermediate $(10^{10} \text{ A} < \text{Current} < 10^{6} \text{ A})$ resistance states can be induced repeatedly, as displayed in FIG. II. 8(c). Intermediate resistance states were induced by applying voltages (2 V, 2.5 V, and 2.7 V; 1 ms) slightly less than 5 V and stable in time: in order to read the resistance state, constant 1 V was applied during 120 seconds. Red, black and blue color circles correspond to FM, intermediate and MG resistance states. 2 V, 2.5 V and 2.7 V were applied to create the intermediate states with $I \approx 10^{-10}$, 10^{-9} and 10^{-8} , respectively. To erase the intermediate resistance states (i.e. going back to the MG phase), two steps were taken: a 5 V pulse was applied to induce the FM phase, and then a large voltage pulse (65 V) was applied to change the FM phase to the MG phase. Note that these fascinating results can be utilized for storing multiple bits on a single memory cell, i.e., multilevel memory applications.

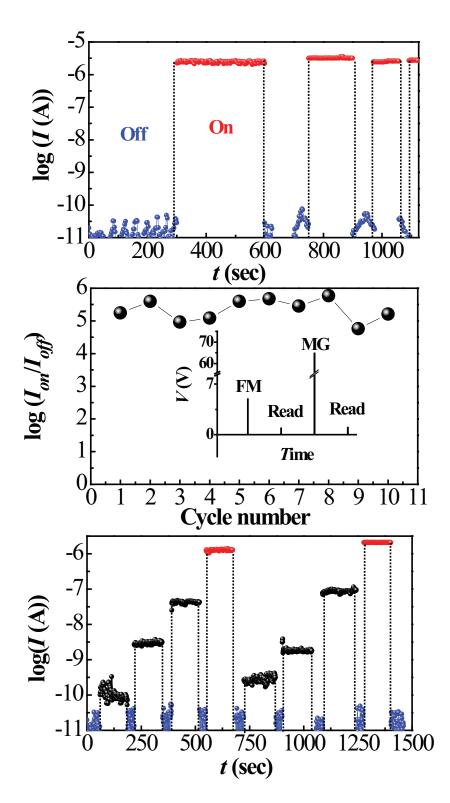


FIG. II. 8 (a) Logarithmic *I*-time (t) plot. (b) Stability of the log (on/off) ratio at 1 V through cycling. (c) Generation of multilevel intermediate resistance states, shown in log(I)-t plot.

4. Conclusions

Low-temperature phases in LPCMO with enormously different resistance values (different by $>10^5$) can be repeatedly switched by applying various voltage pulses. In addition, the resistance value of each phase is highly repeatable through cycling and also stable with time. These behaviors are associated with the intriguing hysteresis in the coexistence of metallic and insulating phases shown in the *V*-*T* phase diagram, and can be utilized for cryogenic memory applications, which can be facilitated in low-*T* electronics technologies. The cooperative freezing of spin/charge/lattice degrees of freedom below ~25 K appears essential for the high stability of induced phases. We also found that phases with intermediate resistance values can be repeatedly induced and switched back to an insulating or metallic phase by applying appropriate voltage pulses, which can be exploited for multilevel memory devices.

5. References

[1] C. H. Bennett, and D. P. Divincenzo, Nature 404, 247 (2000).

[2] P. M. Platzman, and M. I. Dykman, Science 284, 1967 (1999).

[3] R. Prevedel, et al. Nature 445, 65 (2007).

[4] J. Clarke, and F. K. Wilhelm, Nature 453, 1031 (2008).

[5] M. Rodwell, M. high speed integrated circuit technology, towards 100 GHz logic world scientific, Singapore, (2001).

[6] T. Ortlepp, et al., Science **312**, 1495 (2006).

[7] See for example: Superconducting Technology Assessment, National Security Agency office of corporate assessments (NSA)), http://www.nitrd.gov/pubs/nsa/sta.pdf.

[8] A. Peacock, et al., Nature **381**, 135 (1996).

[9] P. K. Day, H. G. LeDuc, B. A. Mazin, A. Vayonakis, and J. Zmuidzinas, Nature 425, 817 (2003).

[10] B. Cabrera, R. M. Clarke, P. Colling, A. J. Miller, S. Nam, and R. W. Romani, Appl. Phys. Lett. **73**, 735 (1998).

[11] S. S. P. Parkin, C. Kaiser, A. Panchula, P. M. Rice, B. Hughes, M. Samant, and S.-H. Yang, Nature Mater. **3**, 862 (2004).

[12] S. R. Ovshinsky, Phys. Rev. Lett. 21, 1450 (1968).

[13] J. Hegedűs, and S. R. Elliott, Nature Mater. 7, 399 (2008).

[14] R. Waser, and M. Aono, Nature Mater. 6, 833 (2007).

[15] A. Baikalov, et al., Appl. Phys. Lett. 83, 957 (2003).

[16] S. C. Chae, *et al.* Adv. Mater. **20**, 1154 (2008).

[17] M. Uehara, S. Mori, C. H. Chen, and S.-W. Cheong, Nature 399, 560 (1999).

[18] P. Levy, F. Parisi, L. Granja, E. Indelicato, and G. Polla, Phys. Rev. Lett. **89**, 137001 (2002).

[19] A. Asamitsu, Y. Tomioka, H. Kuwahara, and Y. Tokura, Nature 388, 50 (1997).

[20] M. Tokunaga, H. Song, Y. Tokunaga, and T. Tamegai, Phys. Rev. Lett. **94**, 157203 (2005).

[21] R. P. Rairigh, G. Singh-Bhalla, S. Tongay, T. Dhakal, A. Biswas and A. F. Hebard, Nature Phys. **3**, 551 (2007).

[22] V. Kiryukhin, D. Casa, J. P. Hill, B. Keimer, A. Vigliante, Y. Tomioka, and Y. Tokura, Nature **386**, 813 (1997).

[23] K. Miyano, T. Tanaka, Y. Tomioka, and Y. Tokura, Phys. Rev. Lett. **78**, 4257 (1997).

[24] H. Y. Hwang, T. T. M. Pastra, S.-W. Cheong, and B. Batlogg, Phys. Rev. B 52, 15046 (1995).

[25] L. Zhang, C. Israel, A. Biswas, R. L. Greene, and A. de Lozanne, Science. **298**, 805 (2002).

[26] W.Wu, C. Israel, N. Hur, S. Park, S. -W. Cheong, and A. de Lozanne, Nature Mater. 5, 881 (2006).

[27] P. A. Sharma, S. B. Kim, T. Y. Koo, S. Guna, and S.-W. Cheong, Phys. Rev. B **71**, 224416 (2005).

Chapter III

Switchable diode and photovoltaic effect in ferroelectric BiFeO₃

1. Introduction

Photodiodes and solar cells are attractive active devices in the arena of green energy and optical devices. Using these, solar energy can be converted directly into electric current flow and light illumination can modulate the current. The conventional description of a common rectifying p-n junction shows the effect to be due to diffusion of carriers across the p-n barrier, inducing an internal electric field. Recently, to enhance the optical device and solar energy harvest functionalities, other types of photovoltaic cells have been widely researched. For example, in excitonic solar cells such as dye-sensitized TiO₂, electron-hole pairs, called excitons, are created by light dissociate at the dye/TiO₂ interfaces and only electrons flow through TiO₂ grains [1-3]. Schottky barrier at the interface between a metal and a semiconductor has also been utilized to create a photovoltaic effect [4].

The bulk photocurrent flow created in ferroelectrics such as LiNbO₃ by UV light illumination depends upon the direction of ferroelectric polarization, leading to a ferroelectric photovoltaic (FPV) effect. The main drawback of this intriguing FPV effect is the tiny magnitude of photocurrent in typically-insulating ferroelectrics [5, 6]. A recent breakthrough has been made in ferroelectric BiFeO₃ (BFO) in which large FPV current is induced by visible light illumination [7]. On the other hand, the mechanism for this remarkable FPV effect in BFO is largely unknown, and technical exploitation has to be pursued. In order to elucidate the origin of this FPV effect in BiFeO₃, we have investigated various photovoltaic configurations with BFO single crystals, and found, for the first time, that 1) the direction of the FPV current is reversibly switchable by applying electric voltage pulses, 2) the switchable Schottky-to-Ohmic barriers mechanism was

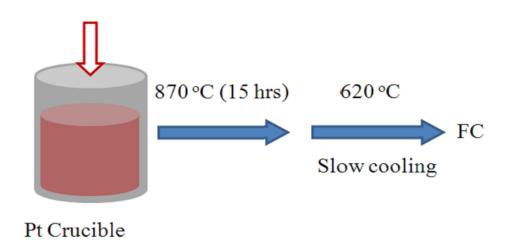
proposed as a possible scenario, 3) bulk photovoltaic effect also confirmed by using four prove resistance measurement and 4) 71° domain wall conduction is observed by using CAFM technique in the single crystal BiFeO₃. These results provide critical insights into understanding and also optimizing the remarkable FPV in BiFeO₃.

2. Experimental Method

BiFeO₃ single crystals were grown using a flux technique with Bi_2O_3 , and B_2O_3 flux [7]. The schematic of flux growth and the picture of BiFeO₃ single crystal which made by flux growth are shown in FIG. III. 1. The XRD (X-ray diffraction data) of ground BiFeO₃. We could not find any impurity and second phase peaks. The XRD of top surface shows only c direction peaks in cubic rotation (FIG. III. 2).

Five plate-like (BFO1; 0.9x0.35x0.06 mm³, BFO2; 1.5x0.8x0.06 mm³, BFO3; 7x2x0.2 mm³, BFO4; 3x0.7x0.08 mm³, BFO5; 1.5x1.3x0.07 mm³) specimens were prepared through cutting and polishing a grown crystal, and the surfaces of the crystal specimen were cleaned with dilute nitric acid and dilute bromine. The specimens were annealed at 673 K in an Ar atmosphere in order to remove strain during polishing. Semitransparent (~20 nm thick) gold electrodes were sputtered on the top and the bottom surfaces, and 2 mil-diameter gold wires were used for electric leads. The top and bottom surfaces of BFO1 were coved with black insulating tape to prevent any light illumination on the electric contacts and to ensure light illumination only on one side surface.

The temperature of the specimen during the experiments was controlled using the Quantum Design Physical Property Measurement System (PPMS). The photocurrent was measured with a Keithley 617 low current multi-meter and the current-voltage



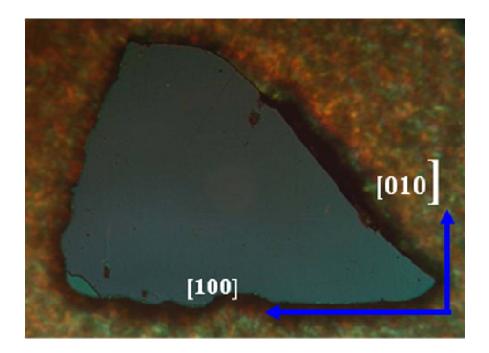


FIG. III. 1. Picture of $BiFeO_3$ single crystal made by flux growth and flux growth recipe for $BiFeO_3$

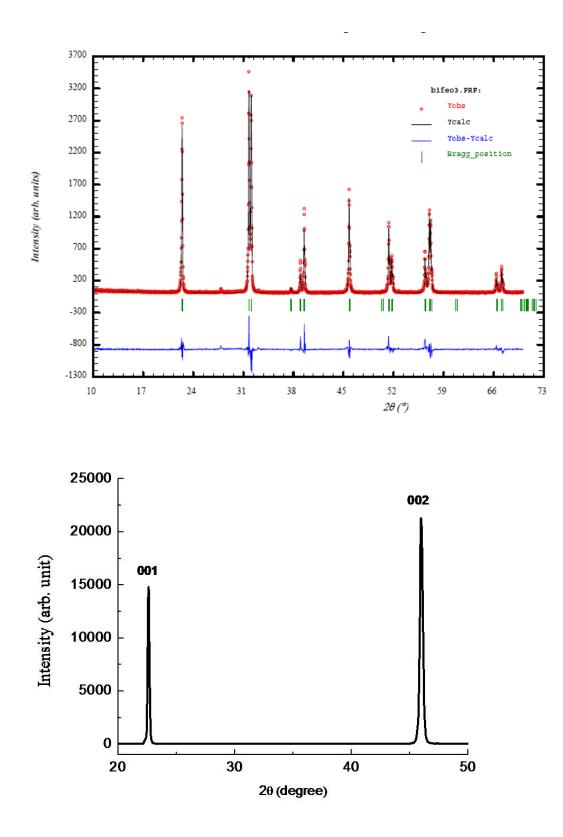


FIG. III. 2. The XRDs of ground BiFeO₃ and top surface of sample.

measurements were performed with a Keithley 2400 source-meter. Current noise level of $\sim 10^{-11}$ A in our current-voltage curves originates from the resolution limit of Keithley 2400. A Veeco microscope was used to obtain AFM and PFM images.

The wavelength dependence of the photocurrent and EQE data were obtained using a monochromatic pulsed light and a lock-in (EG&G 5210 lock-in amplifier) technique. To produce the monochromatic pulsed light in the range of 300-800 nm, we used a 150 W Oriel Q60000 Xe light bulb, an Oriel Cornerstone 130 monochromator, and a chopper. Generalized spectroscopic ellipsometric (g-SE) measurements were performed with the sample at room temperature using a variable-angle rotating compensator-type spectroscopic ellipsometer (M2000-DI model, J.A. Woollam Inc.).

3. Results and Discussion

Using piezoresponse force microscopy (PFM), we have observed ferroelectric polarization switching in a BFO crystal with a cubic orientation. We first found that the entire crystal is in a single ferroelectric domain state with polarization along the cubic [111] direction. PFM-amplitude and phase images show the voltage-induce polarization switching in the single-domain crystal (FIG. III. 3). The dark region in the phase image corresponds to a domain with an upward polarization component after applying a negative voltage to the top electrode, while the white colored region is the original region with a downward polarization component. Both the presence of a rectification effect as well as switching of the rectification direction are observed in our specimen (FIG. III. 4). Two thin plate-like crystals of BFO were prepared: Au electrodes on the out-of-plane surfaces were sputtered to BFO1 and BFO2. To pole the sample, +210 V (10 ms

duration; 120 ms interval) pulses were applied on BFO1 for 2 min at room temperature (positive on the top surface, called positive poling), as shown in the top panel of FIG. III. 4. The rectifying behavior was observed with the top-to-bottom (downward) as the forward bias direction. This demonstrates that the forward bias direction is directly parallel with the induced ferroelectric polarization. One of the side surfaces was illuminated with a green laser (2.33 eV photon energy; $\lambda = 532$ nm, and a power density of ~20mW/cm²).

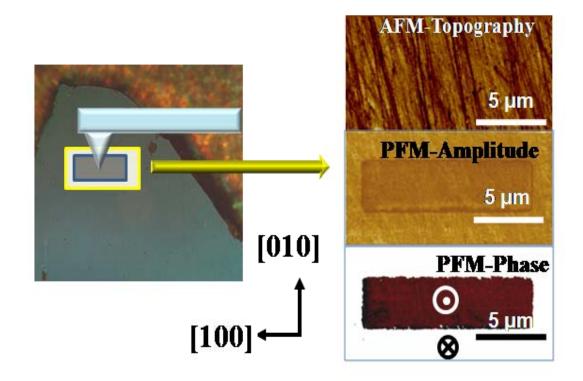


FIG. III. 3. Top to bottom; optical microscope image of our single-ferroelectric-domain $BiFeO_3$ specimen, and AFM topography, PFM amplitude and PFM phase images of the yellow-color-outlined region. A +40 V bias was applied to the bottom electrode in order to induce upward polarization (dark colored region in the PFM phase image). The white colored region in the PFM phase image indicates the original downward-polarization domain.

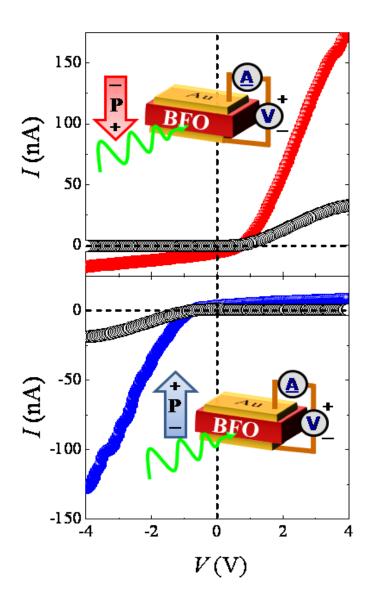


FIG. III. 4. *I-V* curves with downward polarization (top) and upward polarization (bottom). Black open circles are for the *I-V* curves in dark, and red and blue filled circles indicate current under green laser illumination. Cartoon shows the schematic of our experiment setup.

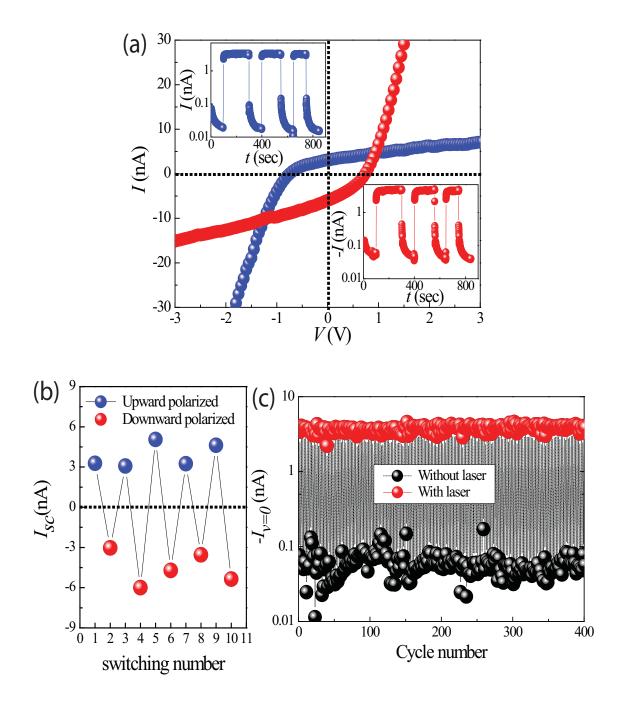


FIG. III. 5(a). Expanded view of the *I*-*V* curves for two different polarization orientations. Insets show zero-bias photocurrent with repetition of light on and off. Blue and red colored data are for upward and downward polarizations, respectively. (b) Zero-bias photocurrent with light on (I_{sc}) with repetition of polarization-orientation switching. (c) I_{sc} with and without light illumination

In order to avoid light illumination on the top and the bottom surfaces, both surfaces were covered by insulating black tape.

The black-colored open circles in the top panel indicate the dark current after poling, and red-colored closed circles show the current-voltage (*I-V*) curve under illumination. To reverse the rectification direction, -210 V (\sim 35 kV/cm) was applied, as shown in the bottom panel of FIG. III. 4. Black-colored open circles in the bottom panel indicate the switched rectification effect, and blue-colored circles show the *I-V* characteristic under the light illumination after the switching.

Remarkable switching of the photovoltaic current direction and good retention of the photovoltaic effect are clearly presented in FIG. III. 5(a). Short circuit currents (I_{sc}) are always opposite to the forward bias direction: I_{sc} after positive poling is negative 4 nA (-1.26 μ A/cm²), whereas I_{sc} after negative poling is about positive 3 nA (+0.95 μ A/cm²). Good retention and high stability over cycling are critical parameters for possible device applications. I_{sc} as a function of time, measured with a 100 ms time step, is shown in the inset of FIG. III. 5(a), which demonstrates little temporal change of photovoltaic current. Switching of the photocurrent direction was also performed 10 times, and the absolute value of I_{sc} is stable over cycling within ~1 nA (FIG. III. 5(b)). Furthermore, we found that there exists no hint of photovoltaic current degradation when I_{sc} was measured during 400 light-on-and-off cycles (FIG. III. 5(c)).

The photovoltaic current measured with varying light frequencies as shown in FIG. III. 6. The onset energy and peak energy in our data are well matched with energies of reported band edge and bandgap. The bandgap of BFO2 has been estimated or measured to be in the range of 2.5–2.8 eV, and the edge of the band gap is 2.1-2.2 eV [8-

12]. Consistent with these properties, the photovoltaic current starts to increase drastically for light energy larger than ~2.2 eV, and peaks at about 2.8 eV with 16 μ A/cm². We have also measured the external quantum efficiency (EQE) of the photovoltaic effect in BFO2. The EQE value exhibits a peak of ~1.5 % at ~2.9 eV. 1.5 % EQE is significantly larger than that of the La doped PZT (0.28 % under UV light), reported as the highest conversion efficiency in ferroelectrics [13].

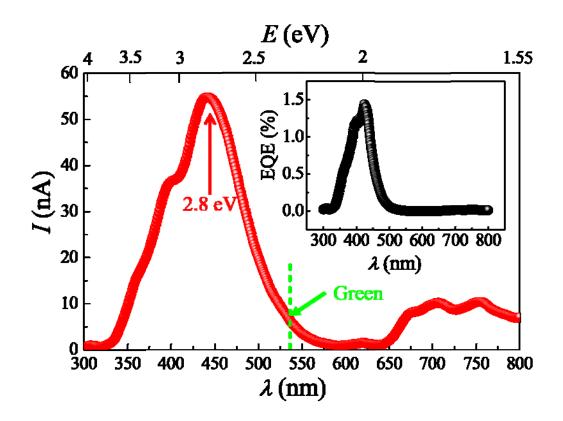


FIG. III. 6. The light wavelength dependence of I_{sc} . I_{sc} becomes maximum at the 2.8 eV and green arrow shows the energy of the green laser used for data in FIG. III. 4 and 5. The external quantum efficiency (EQE) of our BiFeO₃ photocell is shown in the inset.

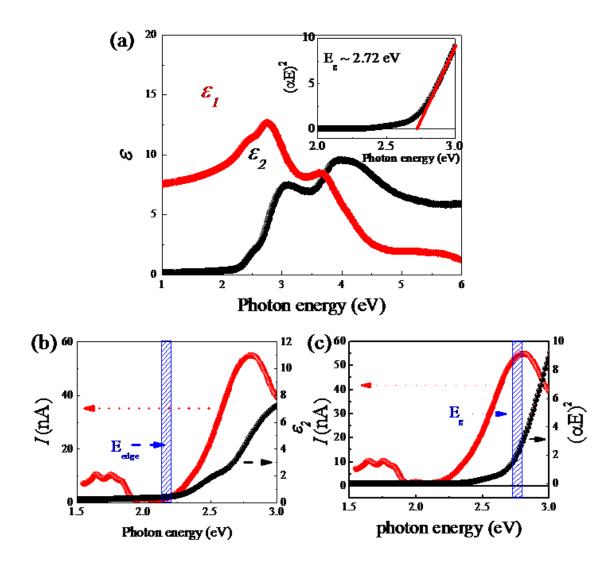


FIG. III. 7. (a) Absorption spectrum data measured by ellipsometry. Epsilon 1 and epsilon 2 are indicated by red and black colored circles. bandgap value was extracted from the $(\alpha E)^2$ in inset figure. (b) ~2.2 eV band edge came from I_{sc} and ε_2 data. (c) comparison of bandgap value extracted from the I_{sc} and $(\alpha E)^2$ data

Absorption spectrum data of BFO3 were also measured by ellipsometry at 300 K as displays in Fig. III. 7. ~2.2 eV band edge was extracted from our epsilon (ε_2) data and ~2.72 eV bandgap was obtained from a linear extrapolation of (αE)² versus photon

energy graph (inset Fig. III. 7(a), (b) and (c)). Little mismatch in band gap obtained ε_2 with I_{sc} maybe origins from the surface roughness and/or optical anisotropy in our single crystal. The kink near 2.5 eV in absorption graph was reported as defect states induced by oxygen vacancies [14,15]. The clear feature near 2.5 eV in Fig. III. 7(b) indicates the relatively large amount of oxygen vacancies compare with BFO film.

A resistivity of the order of $10^{10} \Omega$ cm has been reported for good BFO films with minimal oxygen vacancies, but the resistivity value of ~ $3x10^8 \Omega$ cm has been observed in oxygen-deficient BFO films prepared in low oxygen pressures [16,17]. The low-voltage resistivity of our BFO crystals is of the order of $10^8 \Omega$ cm and the resistivity decreases to an order of $10^7 \Omega$ cm in high voltages. Thus, our BFO crystals appear to have a significant amount of oxygen vacancies which is consistence with our epsilon result.

We have interesting results when we studied the poling-voltage dependence of rectification direction switching. The forming-voltage dependence of the rectification (Fig. III. 8) undoubtedly suggests that polarization flipping is necessary for rectification switching. Starting from the negative rectification state, a slowly-varying DC voltage was applied to BFO1 from zero to the positive maximum forming voltage (V_f), and then back to zero at room temperature. Subsequently, the *I-V* characteristic was measured in a low voltage range (within \pm 5 V). In order to remove unwanted effects such as charging during the forming process, the specimen was discharged before the *I-V* measurement. The forward direction current at -5 V is slightly reduced until V_f=55 V, while the reverse direction current at +5 V sharply increases. The magnitudes of the currents at \pm 5 V cross each other at V_f=60 V, and thus the forward and reverse directions switch each other for V_f>60 V. When V_f was swept beyond 60 V, the decrease of the original-forward-

direction current speeds up while the increase of the original-reverse-direction current slows down. The features at V_f =55-60 V are rather evident, and this voltage (~10 kV/cm) is rather close to the ferroelectric coercivity at room temperature.

We now discuss about possible scenarios for the dynamic switchable diode effect. First, we classify the source of this effect into two distinction: interface effect and bulk effect.

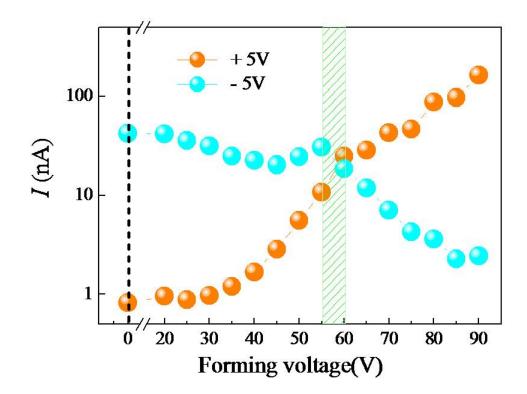


FIG. III. 8. The forming-voltage (V_f) dependence of current. The orange and light blue colored circles indicate the current at + 5 V and - 5 V (maximum applied voltages for the *I-V* curves), respectively, after applying V_f at room temperature. The clear feature at 55-60 V is probably associated with the polarization switching field, demonstrating the importance of polarization flipping for switching the rectification direction.

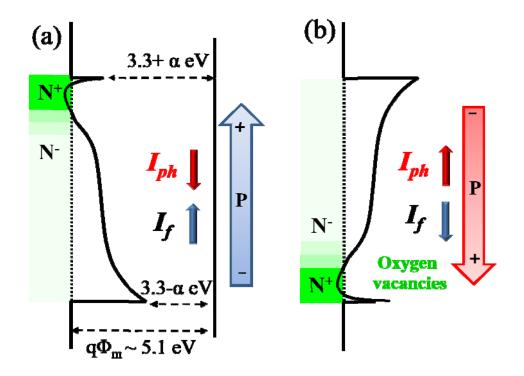


FIG. III. 9 (a), and (b). Schematic energy band diagrams for two different polarization orientations. α and α^* corresponds to the barrier height change induced by, e.g., polarization, Schottky barrier pinning and the charge neutrality level. I_f and I_{ph} are a forward bias current and a zero-bias photocurrent, respectively. $q\Phi_m$ depicts the metal work function. N represents the electron-doped region, and heavy doping in the N⁺ region is due to the presence of defects such as oxygen vacancies, induced by applying forming voltages.

As an interface effect, we consider the possibility of switchable Schottky-to-Ohmic contacts scenario (Fig. III. 9). The Au-BFO interface can have a Schottky barrier, and the barrier height can be estimated to be ~1.8 eV from the difference between the work function of the Au metal (~5.1 eV) and the electron affinity of BFO (~3.3 eV) by the Schottky-Mott rule [23]. When the Schottky barrier pinning factor and the charge neutrality level are taken into account, the Schottky barrier height between Au and BiFeO₃ is reduced to be ~0.93 eV [11]. Evidently, symmetric Schottky-to-Schottky interfaces such as Au/BFO/Au will not induce the observed rectification effect. Now, electron affinity can be naturally influenced by electric polarization in ferroelectrics, inducing the reduction (increase) of the barrier height at the region of the polarization head (tail) [24]. If this barrier height reduction at the polarization head region is sufficient enough, then our Au/BFO/Au specimen can have Schottky-to-Ohmic contacts, which can lead to a rectification effect.

Another way to have Schottky-to-Ohmic contacts is heavy doping at one of the Au/BFO/Au interface, which can lead to tunneling through the barrier. As mentioned before, a large amount of positively charged oxygen vacancies exist in our sample and they migrated and accumulated to the negative electrode side when a high electric field was applied. These accumulated oxygen vacancies are frozen when the electric field is removed. The large parts of voltage drop appear near the contact areas because of the large resistance in there. Then the sample is divided into heavily doped (N⁺) and N regions and N and lightly doped (N⁻) regions. Depletion regions similar to a P-N junction diode are established in the interfaces of the N⁺/N and N/N⁻. This oxygen vacancies in negative part produce a lot of electron charge carriers, which can easily move to the metal contact by the tunneling and/or reduced barrier until equilibrium is reached.

This scenario is schematically depicted in Fig. III. 9, and with the Schottky-to-Ohmic contacts in the figures, the diode forward direction becomes naturally opposite to the zero-bias photovoltaic current direction. Note that with this assumption of Schottkyto-Ohmic contacts (i.e. only one Schottky barrier interface), apparent potential barrier height, Φ_{app} , is estimated from the activation energy behavior of our temperature dependent *I-V* curves, and from the extrapolation of the Φ_{app} vs V^{1/2} curve [23,25], the barrier height is extracted to be ~ 0.46 eV. This value is somewhat smaller than the theoretical estimation of ~ 0.93 eV [11], suggesting the limit of our simple contact-effect model.

As a bulk effect, three scenarios are available: optical rectifying effect, graded distribution of traps and space charge limited conduction (SCLC) mechanisms [7,26-30]. In the optical rectifying effect case, the nonlinear optical processes probably cannot explain the diode effect in dark. In the graded distribution of traps case, positively charged oxygen vacancies exist in our sample and they migrated and accumulated to the negative electrode side when a high electric field is applied. If the large electric field is applied uniformly through the bulk area, the trap density increases monotonically with distance from positive side. The schematic draw is shown in Figure. III. 10.

Finally, SCLC mechanism by asymmetric impurity potential case, asymmetry traps can be appeared by chemical impurity such as oxygen vacancies in ferroelectric matrix. The higher barrier of impurity potential is located in polarization head side while the lower barrier is located in polarization tail side as shown in Fig. III. 11 and which asymmetric barrier can be switched by poling opposite direction [24, 26]. Free carriers induced by shallow impurities and defects can be present in BiFeO₃, and can induce the Ohmic behavior ($J \propto E^1$) in low applied voltage. For large applied voltage, injected carrier density exceeds the free carrier density, and SCLC associated with deep trap centers become playing a main role. As a part of deep traps become filled, the abrupt increasing of current observed with increasing applied voltage. It is so called trap-filled limited region ($J \propto E^n$, with n>2). Further carrier injection with increasing the applied field more, injected carriers fill the all trap centers, and thus enter to trap-free space charge limited

conduction which leasing to square law characteristic($J \propto E^2$).

At low bias voltage, slopes of 1 and 0.7 are observed in our BiFeO₃ log- log plot for forward and reverse directions respectively. When the applied voltage is increased (small V), the forward direction enters the trap-filled limited region with the n value of 5. Meanwhile, there is no slope change in reverse direction. As the applied voltage is increased further (large V), a trap-free space charge limited conduction regime is followed with the n value of 2.3 (forward direction) and 2.4 (reverse direction) [7].

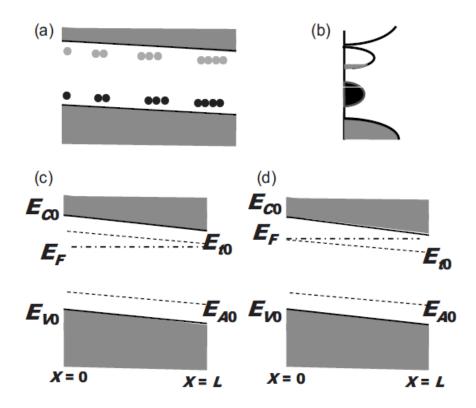


FIG. III. 10. (a) Schematic drawing of gradient trap-density distribution (b) the corresponding band profile (c) shallow-trap and (d) deep-trap case [27].

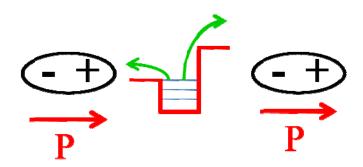


FIG. III. 11. Schematic drawing of asymmetric potential by oxygen vacancy in polarized material. Large current direction is consistent with polarization direction because electrons easily trap out into lower barrier side [26].

We are now interested verifying experimentally whether or not the RPV effect in BFO is related with a bulk effect. The four probe measurement is a most useful tool to check the bulk diode effect. In order to observe bulk behavior under electric polarity, BFO4 sample was prepared as depicted in the inset figure in the Fig. III. 12. To pole the sample to downward, positive 210 V pulses were applied from contact 4 (P4) to contact (P1) and the rectifying effect by two probe measurement was observed. The four probe voltage measured between contact 3 (P3) and contact 4 (P4) with change applied current between P4 and P1. The diode effect was observed and the forward direction is consistent with that of two probe measurement. To confirm the effect, the sample poled to upward by applying negative 210 V. and the diode effect also changed as shown in Fig. III. 12.

Another four probe measurement was also measured with different sample BFO4. The geometry of sample and contact is depicted in the inset figure in the Fig. III. 13. The two probe data between top contact (T1) and bottom contact (B1) and the four probe data between T2 and B2 are nicely show the diode effect. In order to measure 4 probe measurement, current applied between T1 and B1 and the voltage drop measured between T2 and B2. Our four point probe data show clearly bulk diode effect.

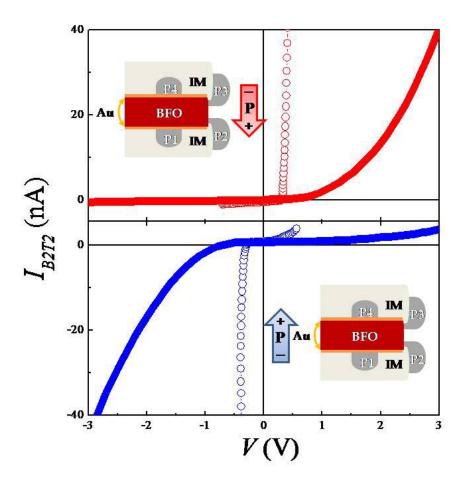


FIG. III. 12. Schematic draw of sample preparation and two probe and four probe I-V characteristic data. Closed circles and opened circles indicate two probe between P4 and P1 and four probe between P3 and P2 respectively. Downward and upward poling cases are distinguished by red and blue color respectively.

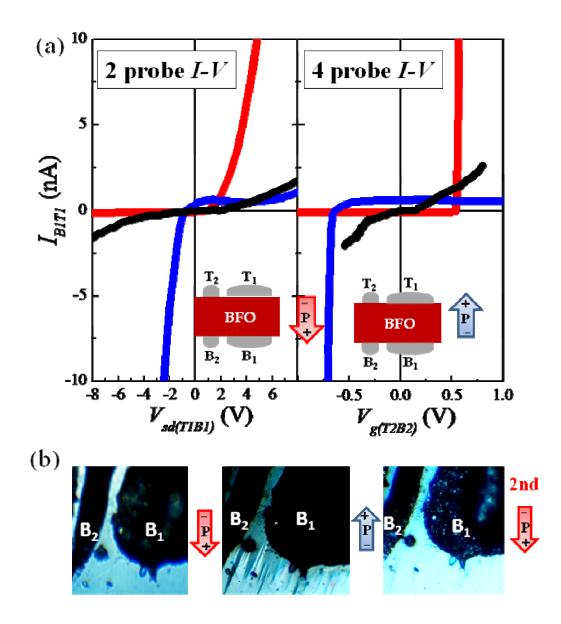


FIG. III. 13. (a) schematic draw of sample preparation and two probe and four probe I-V characteristic data. Downward and upward poling cases are distinguished by red and blue color respectievely. Black colored circles indicate symmetry case. The distance between T1 (B1) and T2 (B2) is ~30 μ m (b) Optical microscope image after poling. The sequence is downward \rightarrow upward \rightarrow downward.

During the poling, interesting feature was observed by optical microscope. As shown in Fig. III. 13(b), spike like features appear near top and bottom contact during upward poling and that feature disappeared by downward poling. In order to figure it out, AFM, PFM and CAFM techniques were applied in BFO5. Au contacts were sputtered both on the top and the bottom surfaces. By downward poling, spike like feature observed outside of Au contact as shown in the optical microscope picture in the Fig. III. 14 and that feature keep spread out by increasing the poling time.

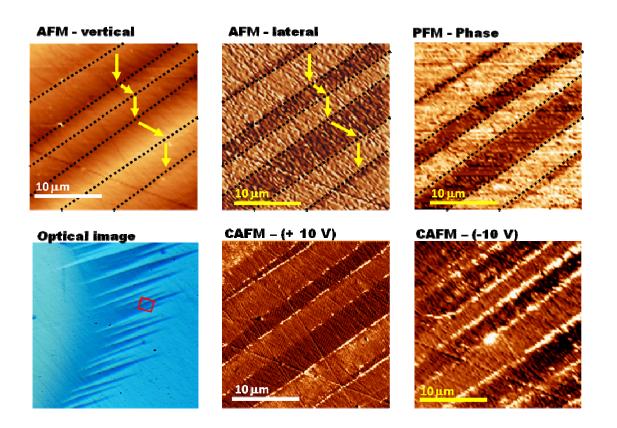


FIG. III. 11. AFM, PFM, CAFM and optical images of BFO5. Yellow arrows indicate the polarization directions. Bright color in CAFM image indicates high current flow.

The AFM vertical and lateral images clearly show the mountain and valley like features on the surface. The brightest areas and darkest areas in the vertical AFM image point out highest height and lowest height regions respectively. The bright areas in the lateral image indicate uphill, while dark areas indicate downhill. The PFM image is matched perfectly with that mountain and valley like features on the surface. It indicates the polarization flipping in an uphill area, which is connected with the Au contact, like Fig. III. 3. The inversion of the conduction between the domains also was observed by Conducive AFM (CAFM). The bright color indicates high current flow and the dark color indicates less current flow in CAFM image. The brightest lines between domains show obviously the domain wall conduction, while observed domain conduction is not clear because of that observed currents are near noise level and that noise level conduction can be induced by surface or charging of tip.

4. Conclusions

In summary, a significant rectification accompanies the FPV effect in BFO, and the direction of the rectification and photovoltaic current is reversely switchable by large external voltages. The forward bias direction is along the ferroelectric polarization direction and short circuit currents after positive poling is $-1.26 \,\mu\text{A/cm}^2$, whereas I_{sc} after negative poling is $+0.95 \,\mu\text{A/cm}^2$ with a good retention and high stability over cycling. We confirmed that the polarization clearly plays an essential role in the rectification and photovoltaic effects by PFM and poling-voltage dependence of rectification direction switching measurement. The rectification effect is consistent with the presence of Schottky-to-Ohmic contacts, and the Schottky-to-Ohmic contacts appear to be switchable with external voltages. The switching of Schottky-to-Ohmic contacts results from a combined effect of polarization flipping and electromigration of defects (oxygen vacancies) from one contact to the other. To verify an existence of the bulk diode effect, four probe measurements were performed in BFO sample and the rectification effect was observed clearly. As a mechanism of the bulk rectification effect, graded distribution of traps and SCLC mechanism were discussed. Further study of these effects, such as experiments involving different ferroelectric materials and controlled doping levels will be necessary to unveil the true origin. We also found that bulk absorption across the band gap determines the photovoltaic effect, and that external quantum efficiency of our simple device can be as large as ~1.5 % at ~2.9 eV. With this in mind, we consider BFO as a FPV material with a switchable diode direction. If engineered by band gap, carrier concentration, and device configurations, this novel "switchable diode and photovoltaic effects" has the advantage of producing photocoltaic and rectification effects while being a ferroelectric: giving fast state read-outs, and acting as a sensor or photocell.

5. References

[1] B. O'Regan, and M. Grätzel, Nature 353, 737 (1991).

[2] U. Bach, D. et al., Nature **395**, 585 (1998).

[3] C. S. Karthikeyan, H. Wietasch, and M. Thelakkat, Adv. Mater. 19, 1091 (2007).

[4] H. C. Card, E. S. Yang, and P. Panayotatos, Appl. Phys. Lett. 30, 643 (1977).

[5] A. M. Glass, D. von der Linde, and T. J. Negran, Appl. Phys. Lett. 25, 233 (1974).

[6] G. Dalba, Y. Soldo, F. Rocca, V. M. Fridkin, and Ph. Sainctavit, Phys. Rev. Lett. 74, 988 (1995).

[7] T. Choi, S. Lee, Y. J. Choi, V. Kiryukhin, and S.-W. Cheong, Science. **324**, 63 (2009).

[8] S. R. Basu, et al., Appl. Phys. Lett. 92, 091905 (2008).

[9] J. F. Ihlefeld, et al., Appl. Phys. Lett. 92, 142908 (2008).

[10] F. Gao, Y. Yuan, K. F. Wang, X. Y. Chen, F. Chen, J.-M. Liu, and Z. F. Ren, Appl. Phys. Lett. **89**, 102506 (2006).

[11] S. J. Clark, and J. Robertson, Appl. Phys. Lett. 90, 132903 (2007).

[12] X. S. Xu, et al., Phys. Rev. B 79, 134425 (2009).

[13] M. Qin, K. Yao, and Y. C. Liang, Appl. Phys. Lett. 93, 122904 (2008).

[14] C. Himcimschi, et al., J. Appl. Phys. 107, 123524 (2010)

[15] A.J. Hauser, et al., Appl. Phys. Lett. 92, 222901 (2008)

[16] W. Eerenstein, F. D. Morrison, J. Dho, M. G. Blamire, J. F. Scott, and N. D. Mathur, Science. **307**, 1203a (2005).

[17] Y. W. Li, et al., J. Phys. D 41, 215403 (2005).

[18] C.-H. Yang, et al., Nature Mater. 8, 485 (2009).

[19] R. Mogilevsky, et al., Phys. Rev. B 49, 6420 (1994).

[20] M. Janousch, G. I. Meijer, U. Staub, B. Delley, S. F. Karg, and B. P. Andreasson, Adv. Mater. **19**, 2232 (2007).

[21] Guo-Liang Yuan, and Junling Wang, Appl. Phys. Lett., 95, 252904 (2009).

[22] M. Quintero, P. Levy, A. G. Leyva, and M. J. Rozenberg, Phys. Rev. Lett. 98, 116601 (2007).

[23] S. M. Sze, *Physics of Semiconductor Device*, (Wiley-Interscience, New York, 1981).

[24] P. Maksymovych, S. Jesse, P. Yu, R. Ramesh, A. P. Baddorf, and S. V. Kalinin, Science. **324**, 1421 (2009).

[25] I. Vrejoiu, D. Hesse, G. LeRhun, M. Alexe, Phys. Rev. B 75, 104103 (2007).

[26] M. E. Lines, A. M. Glass, *Principles and Applications of Ferroelectrics and Related Materials* (oxford, 1979)

[27] Y. Watanabe, Phys. Rev. B 81, 195210 (2010).

[28] K. Tonooka, P. Poosanaas, and K. Uchino, Proc. SPIE 3324, 224 (1998).

[29] M. Gass, P. A. Franken, J. F. Ward, and G. Whinreich, Phys. Rev. Lett. 9, 446 (1962).

[30] A. Rice et al., Appl. Phys. Lett. 64, 1634 (1994).

Chapter IV

Multiferroicity in an 1D Ising Chain Magnet

Ca₃CoMnO₆

1. Introduction

The concept of magnetism-driven ferroelectricity has recently drawn a significant attention as a Multiferroics [1,2]. Magnetism and ferroelectricity are widely used in current technology such as a non-volatile memories, capacitors, memory storage, transducers, actuators and even ferroelectric photovoltaic devices. There is an enormous technological development if these two fascinating characters co-exist. Additional degrees of freedom in device functionality can be provided and also multistate memory devices can be realized. The multiferroics: the electric polarization effected by applying magnetic field and magnetization can be changed by applying electric field. To achieve it, blending method used such as attach two materials one is piezoelectric and magnetostrict. When a magnetic field is applied to the composites, firstly, there is a shape change in magnetostrictive material and then the mechanical stress is passed though the piezoelectric material. As a result, the electric polarization changed. In magnetismdriven ferroelectrics, development of inversion-symmetry-breaking magnetic order leads to the loss of the lattice inversion symmetry through exchange striction, thereby leading to the development of ferroelectricity. In these materials, external magnetic field influences the configuration of the magnetic order, naturally leading to changes in ferroelectric or dielectric properties. Spectacular cross-coupling effects, such as reversible flipping of ferroelectric polarization or drastic change of dielectric constant in applied magnetic fields, have been recently observed in magnetism-driven ferroelectrics [3-5]. Spiral magnetic order, resulting from magnetic frustration, is a common way to induce the loss of inversion symmetry, and ferroelectricity has been recently observed in a number of spiral magnets such as TbMnO₃, Ni₃V₂O₈, CuFeO₂, (Ba,Sr)₂Zn₂Fe₁₂O₂₂,

 $CoCr_2O_4$, MnWO₄, and LiCu₂O₂ [6-12]. In the spiral magnets, the relevant exchange striction is associated with the antisymmetric part of the exchange coupling, which constitutes the so-called Dzyaloshinski-Moriya (DM) interaction [13-16].

Spiral magnetic order is not the only possible route towards magnetism-induced ferroelectricity. In RMn_2O_5 (R=Tb – Lu), for example, a nearly-collinear acentric magnetic order with broken inversion symmetry was proposed to be responsible for the ferroelectricity [17]. In this mechanism, the ferroelectricity results from lattice relaxation through exchange striction associated with the symmetric superexchange coupling. However, a model where ferroelectricity is induced by a spiral spin configuration along the Mn^{4+} spin chain has been also discussed for RMn_2O_5 [18,19]. Thus, the true origin of multiferroicity in RMn_2O_5 is currently uncertain. Another promising example is the socalled E-type magnetic order. This collinear order, combined with alternating oxygen cage rotations, has been suggested as the origin of ferroelectricity in the orthorhombic HoMnO₃ [20]. Polycrystalline HoMnO₃ has been experimentally studied to test this theoretical prediction [21], but the induced polarization turned out to be too small to support the proposed theory. Identification of non-spiral magnetism-driven ferroelectrics remains, therefore, an important task. Among those, systems driven by the potentially large symmetric superexchange are, clearly, of special interest.

A simple and conceptually important model in which a collinear spin order induces ferroelectricity through symmetric superexchange can be constructed using an Ising spin chain with competing nearest-neighbor ferromagnetic (J_F) and next-nearestneighbor antiferromagnetic (J_{AF}) interactions [2]. For $|J_{AF}/J_F|>1/2$, the ground-state magnetic order is of the up-up-down-down ($\uparrow\uparrow\downarrow\downarrow\downarrow$) type [22]. If the charges of magnetic ions alternate along the chain, this magnetic ordering breaks inversion symmetry on magnetic sites and can induce electric polarization via exchange striction. The exchange striction associated with symmetric superexchange shortens the bonds between the parallel spins, while stretching those connecting the antiparallel spins. As a result, electric polarization, P, is induced in the direction of the chain. There are two ways to combine the $\uparrow\uparrow\downarrow\downarrow$ order with the ionic charge order, giving rise to the opposite electrical polarization vectors. Experimental realization of such a simple model system would be of a significant importance in the field. Herein, we report discovery of a chain magnet in which this model is remarkably realized.

2. Experimental Method

To find the appropriate experimental system, we have identified $Ca_3Co_2O_6$ derived compounds as possible candidates because $Ca_3Co_2O_6$ is an Ising chain magnet where about a half of Co ions can be replaced by Mn ions [23,24]. The structure of $Ca_3Co_{2-x}Mn_xO_6$ contains spin chains consisting of magnetic ions with alternating oxygen cages of face-shared trigonal prisms and octahedra along the *c* axis. The spin chains are separated by Ca ions, and form a triangular lattice in the *ab* plane. Mn ions have a strong tendency to avoid the trigonal prismatic oxygen coordination. Thus, for example, for x=1, all the Co ions are located in the trigonal prismatic sites, and all the Mn ions occupy the octahedral sites [24]. We prepared single-phase polycrystalline $Ca_3Co_{2-x}Mn_xO_6$ with x up to 1 by using standard solid state reaction method [23]. Since single crystals are necessary for conclusive measurements of the ferroelectric properties, we have attempted to grow single crystals of $Ca_3(Co_2Mn_2O_6$ by utilizing the known technique (KCl-K₂CO₃ flux method) for the growth of $Ca_3Co_2O_6$ crystals [25]. With increasing Mn concentration, the crystal growth was found to be increasingly more difficult. However, single crystals with maximum x approaching 0.96 (as determined by comparing x-ray diffraction patterns of crushed crystals with those of polycrystalline samples) were grown successfully.

DC magnetic susceptibility (χ =*M*/*H*) was measured in a SQUID magnetometer, specific heat (*C*) and AC magnetic susceptibility (χ' and χ'') measurements were carried out in he Quantum Design PPMS, and dielectric constant (ε) was measured using an LCR meter at *f*=44 kHz. The temperature (*T*) dependence of electric polarization (*P*) was obtained by the integration of pyroelectric current with the *T* variation of 2 K/min after poling a specimen from 40 K to 2 K in a static electric field of $E\approx6.7$ kV/cm. For ε and *P* measurements, a *c*-axis needle-shaped crystal was cut and polished with the *ab* plane cross-section of ~0.64 mm² and thickness of ~0.15 mm, and then annealed at 650 °C for 5 hours to remove strain built up during polishing. Neutron powder diffraction measurements were performed on polycrystalline Ca₃Co_{2-x}Mn_xO₆ (x=0.95) at the BT-1 beamline at NIST Center for Neutron Research. Monochromatic neutrons (λ =2.079 Å) were produced by a Ge(311) monochromator, and the data were collected for *T*=1.4, 8, and 20 K.

3. Result and Discussion

Search for the ferroelectricity was performed in the crystal with the highest Mn concentration, x=0.96, and ferroelectric polarization along the chain direction was indeed found. FIG. IV. 1 shows that the polarization smoothly emerges below the transition

temperature of 16.5 K, increases rapidly below ~10 K, and reaches ~90 μ C/m² at 2 K. The appearance of the polarization at 16.5 K coincides with the onset of the magnetic order, which is signified [24] by a broad peak in the magnetic susceptibility, $\chi(T)$, shown in FIG. IV. 2(a). Specific heat also exhibits an upturn at this temperature. The temperature dependence of the dielectric constant along the *c* axis, $\varepsilon_c(T)$, starts deviating from its high-temperature behavior at the onset temperature of the polarization without showing any sharp anomaly, see FIG. IV. 2(b). Instead, $\varepsilon_c(T)$ reveals a broad peak at ~8 K followed by a sharp decrease at lower temperatures. The electric polarization decreases in a magnetic field applied along the *c* axis. There is an additional magnetic anomaly at $T\approx3$ K, which can be seen in the behavior of the derivative $d\chi(T)/dT$ shown in FIG. IV. 2(a); it is discussed in more detail below. The Ising character of this compound is clearly reflected in the large anisotropy of $\chi(T)$.

Studies of Ca₃Co_{2-x}Mn_xO₆ polycrystalline samples suggest that a similar behavior is expected in a wide range of x near x=1. FIG. V. 5(a) and (b) display $\chi(T)$ and $\varepsilon(T)/\varepsilon(T=20 \text{ K})$ for various Mn concentrations, x=0.85, 0.9, 0.95 and 1.0. These data exhibit the same features as those of the corresponding quantities of the x=0.96 single crystal, strongly suggesting that the observed properties of the single crystal are representative for large Mn concentrations. The temperatures of the maxima in $\chi(T)$ and $\varepsilon(T)$, shown in the insets in FIG. IV. 3(a) and (b), decrease with increasing x, indicating the corresponding decrease in the magnetic transition temperature. The corresponding temperatures in the single crystal (dotted lines in the insets) agree well with the Mn concentration x=0.96, corroborating our x-ray results.

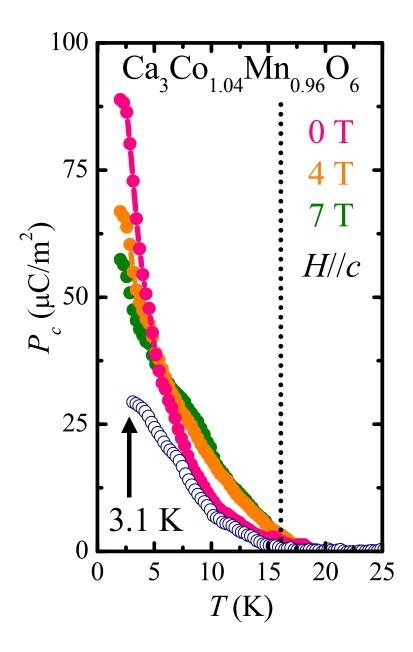


FIG. IV. 1. Electric polarization of single crystal $Ca_3Co_{1-x}Mn_xO_6$ (x=0.96) along the chain direction (*P*//*c*), taken upon warming. The samples were poled upon cooling from 40 K to 2 K (filled circles), and to 3.1 K (open circles) before the measurement. The data for the 2 K poled sample were collected in various applied magnetic fields, as shown.

The structure of Ca₃Co_{2-x}Mn_xO₆ (x=0.95) was determined using neutron powder diffraction. The possible magnetic structures (including those with *ab*-plane components) were constructed using the magnetic symmetry analysis, and the diffraction data were refined using the FULLPROF program package [26]. The spins point along the *c* axis, as indicated by the absence of (003) magnetic peak, and the structure is of the $\uparrow\uparrow\downarrow\downarrow$ type. The accuracy of the final refinement result was independently estimated by the Simulated Annealing process, which shows that the deviation of the spins from the *c* axis cannot exceed 3°. The refinement results for *T*=1.4 K are shown in FIG. V. 6: good agreement factors, $\chi^2 = 1.44$, $R_B = 2.4$ %, $R_f = 2.7$ %, and $R_{mag} = 9.8$ %, are obtained. The obtained three-dimensional magnetic structure is shown in the inset in FIG. IV. 4. In agreement with [24], the Mn ions occupy the octahedral sites. The ordered magnetic moments of Co and Mn ions are 0.66(3) μ_B and 1.93(3) μ_B , respectively, and the estimated valences of the cations from Bond-Valence calculation are 1.814(2) for Co and 3.997(3) for Mn. Thus, the magnetic chains consist of alternating low-spin Co²⁺ and high-spin Mn⁴⁺ ions.

Combined with the $\uparrow\uparrow\downarrow\downarrow$ spin order, this makes Ca₃(Co,Mn)₂O₆ an experimental realization of the magnetoelectric model system described above. In the unit cell shown in FIG. IV. 4, all the chains possess the same polarization direction according to this model. We note that the (101) magnetic peak appears to be slightly broadened (see the inset in FIG. IV. 4. This indicates that the magnetic order is not truly long-ranged. Measurements on yet unavailable large single crystals are needed to determine the magnetic correlation length with any adequate precision. On warming to *T*=8 K, no qualitative changes are observed in the magnetic structure, and no magnetic order is present at *T*=20 K.

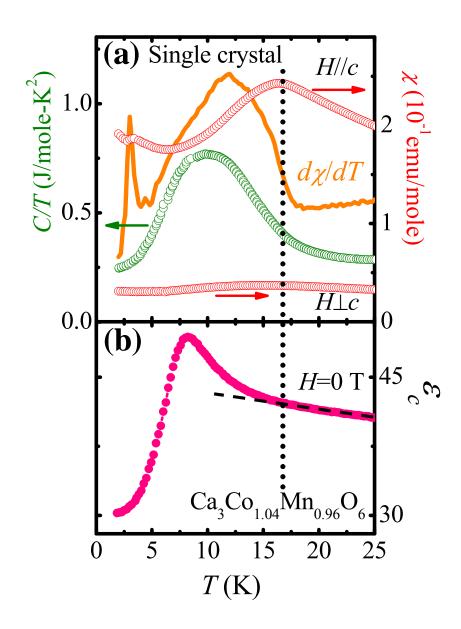


FIG. IV. 2. (a) Temperature dependence of magnetic susceptibility, $\chi(T)=M/H$, measured in an applied magnetic field H=0.2 T along and perpendicular to the chain direction. The temperature derivative $d\chi/dT$, and zero-field heat capacity (C/T) are also shown. (b) The *c*-axis dielectric constant, ε_c . Dashed line shows the high-temperature behavior of ε_c .

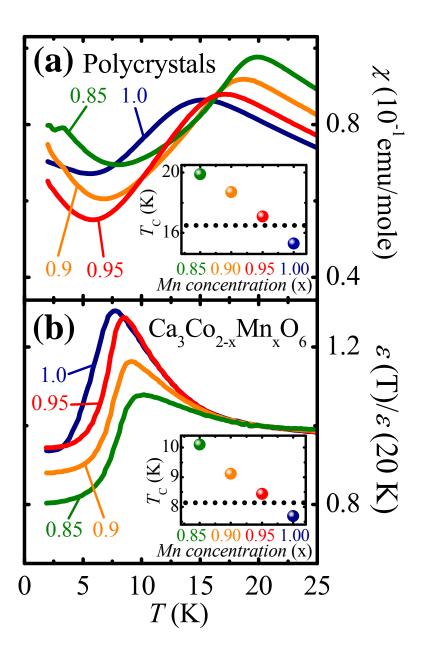


FIG. IV. 3. (a) $\chi(T)$ of polycrystalline Ca₃Co_{1-x}Mn_xO₆ for *H*=0.2 T. (b) $\varepsilon(T)$ of polycrystalline Ca₃Co_{1-x}Mn_xO₆ for *H*=0, normalized at *T*=20 K. The insets in (a) and (b) show peak positions of $\chi(T)$ and $\varepsilon(T)$, respectively, for different Mn concentrations. The dashed lines indicate the corresponding peak positions in the x=0.96 single crystal.

While the magnetic origin of the ferroelectricity, and its description in the framework of the $\uparrow\uparrow\downarrow\downarrow$ chain with alternating ions, are established by the above data, the temperature dependences of both the electric and the magnetic properties are rather complicated. To gain insight into this complexity, we have measured temperaturedependent AC magnetic susceptibility in the x=0.96 single crystal. FIG. IV.5 (a) and (b) reveal that both of the magnetic temperature anomalies (peaks) exhibit strong frequency indicative of magnetic freezing, which may range from simple superparamagnetism to complex spin-glass transition [27]. As shown in the inset in FIG. IV. 5(a), the lowertemperature peak T_{max} of $\chi'(T)$ exhibits the Arrhenius behavior, $f=f_0 exp[-E_a/k_B T_{max}]$, with physically reasonable values of the activation energy, $E_a/k_B \approx 60$ K, and $f_0 \approx 60$ MHz [27]. This behavior with $E_a/T_{max} \approx 20$, together with the numerical value of the slope parameter $\Delta T_{max}/T_{max}\Delta ln[f]$ of 0.21, signals superparamagnetic blocking (freezing of poorlycorrelated magnetic clusters) at low temperatures [27]. The behavior of the highertemperature anomaly, associated with the magnetic ordering transition, is more complicated. For example, T_{max} (>16 K) of $\chi'(T)$ does not exhibit the simple Arrhenius behavior (see the inset of FIG. V. 7(a)). The data of FIG. V. 7, combined with the neutron data, show that only finite-size magnetic domains develop at the magnetic transition, and that these domains exhibit an additional freezing at a lower temperature. This behavior deserves further investigation since it is likely related to the one dimensionality of the magnetic chains and the geometrical frustration in the *ab*-plane triangular lattice.

While complicated, the observed magnetic behavior provides a consistent explanation of the unconventional temperature dependence of the electric polarization in FIG. IV. 1. Magnetic disorder and freezing naturally lead to the corresponding

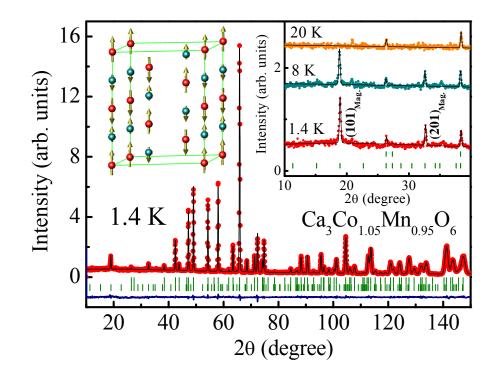


FIG. IV. 4. Observed (symbols) and calculated (line) powder neutron diffraction patterns for polycrystalline $Ca_3Co_{1-x}Mn_xO_6$ (x=0.95) for *T*=1.4 K. The first row of bars below the diffraction pattern indicates the positions of the nuclear Bragg peaks and the second row depicts the locations of the magnetic Bragg peaks. The blue line shows the difference between the observed and calculated diffraction patterns. The insets show the low-angle patterns for *T*=1.4 K, 8 K and 20 K, and the refined spin structure.

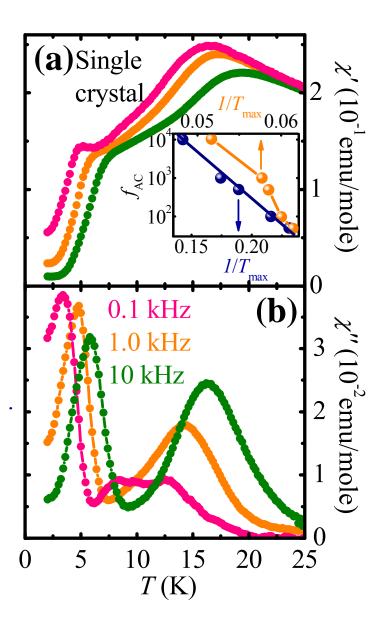


FIG. IV. 5. (a) and (b) Real and imaginary parts of the AC susceptibility, $\chi'(T)$ and $\chi''(T)$, of the x=0.96 single crystal. The AC magnetic field is 5 Oe, and the frequencies are 0.1, 1 and 10 kHz, as shown. The inset in (a) shows $\log[f]$ vs. inverse temperature for the peak-like features of χ' . The low-temperature feature is shown with blue dots, and the high-temperature feature with orange dots.

phenomena for the ferroelectric properties in our system. Local clusters exhibiting the two different variants of the spin order give rise to the opposite electrical polarization vectors. Thus, on warming from 2 K, the frozen poled magnetoelectric domains should quickly become dynamic, leading to decreased macroscopic polarization. This is consistent with the rapid reduction of the polarization with increasing temperature. An additional confirmation of this scenario is obtained by observation of thermal history effects, which are characteristic to frozen states. As shown in FIG. IV. 1, the polarization of the system poled on cooling down to T=2 K (filled circles) significantly exceeds the polarization of the sample poled at T=3.1 K (open circles), when the polarization is subsequently measured on warming in zero field. This is a typical behavior of a frozen system undergoing slow relaxation processes. This scenario is also consistent with the absence of any sharp anomaly of $\varepsilon_c(T)$ at the magnetic transition. We conclude, therefore, that in Ca₃(Co,Mn)₂O₆, thermal fluctuations of the magnetoelectric clusters tend to suppress the macroscopic polarization, leading to the complex temperature dependences and thermal history effects observed in the experiments.

4. Conclusion

We report discovery of an unambiguous example of magnetism-driven ferroelectricity with a collinear magnetic order in the Ising chain magnet $Ca_3Co_{2-x}Mn_xO_6$ (x \approx 0.96). The ferroelectricity originates from the simultaneous presence of the alternating order of Co and Mn ions and the spin order with the $\uparrow\uparrow\downarrow\downarrow\downarrow$ configuration. This provides the first experimental realization of theoretically predicted ferroelectricity in a frustrated Ising chain with an ionic order. Unlike in well-known spiral magnetoelectrics, symmetric exchange striction is expected to drive the ferroelectricity in this system.

5. References

[1] D. I. Khomskii, J. Magn. Magn. Mater. 306, 1 (2006).

[2] S-W. Cheong and M. Mostovoy, Nature Mater. 6, 13 (2007).

[3] N. Hur, S. Park, P. A. Sharma, J. S. Ahn, S. Guha, and S.-W. Cheong, Nature **429**, 392 (2004).

[4] T. Goto, T. Kimura, G. Lawes, A. P. Ramirez, and Y. Tokura, Phys. Rev. Lett. **92**, 257201 (2004).

[5] N. Hur, S. Park, P. A. Sharma, S. Guha, and S.-W. Cheong, Phys. Rev. Lett. **93**, 107207 (2004).

[6] T. Kimura, T. Goto, H. Shintani, K. Ishizaka, T. Arima, and Y. Tokura, Nature **426**, 55 (2003).

[7] G. Lawes, A. B. Harris, T. Kimura, N. Rogado, R. J. Cava, A. Aharony, O. Entin-Wohlman, T. Yildirim, M. Kenzelmann, C. Broholm, and A. P. Ramirez, Phys. Rev. Lett. **95**, 087205 (2005).

[8] T. Kimura, J. C. Lashley, and A. P. Ramirez, Phys. Rev. B 73, 220401(R) (2006).

[9] T. Kimura, G. Lawes, and A. P. Ramirez, Phys. Rev. Lett. 94, 137201 (2005).

[10] Y. Yamasaki, S. Miyasaka, Y. kaneko, J.-P. He, T. Arima, and Y. Tokura, Phys. Rev. Lett. **96**, 207204 (2006).

[11] K. Taniguchi, N. Abe, T. Takenobu, Y. Iwasa, and T. Arima, Phys. Rev. Lett. 97, 097203 (2006).

[12] S. Park, Y. J. Choi, C. L. Zhang, and S.-W. Cheong, Phys. Rev. Lett. **98**, 057601 (2007).

[13] H. Katsura, N. Nagaosa, and A. V. Balatsky, Phys. Rev. Lett. 95, 057205 (2005).

[14] M. Mostovoy, Phys. Rev. Lett. 96, 067601 (2006).

[15] I.A. Sergienko, and E. Dagotto, Phys. Rev. B 73, 094434 (2006).

[16] A. B. Harris, T. Yildirim, A. Aharony, and O. Entin-Wohlman, Phys. Rev. B 73, 184433 (2006).

[17] L. C. Chapon, P. G. Radaelli, G. R. Blake, S. Park, and S.-W. Cheong, Phys, Rev. Lett. **96**, 097601 (2006).

[18] Y. Noda et al., Physica B 385-386, 119 (2006).

[19] H. Kimura et al., J. Phys. Soc. Jpn. 75, 113701-1 (2006).

[20] I. A. Sergienko, C. Sen, and E. Dagotto, Phys. Rev. Lett. 97, 227204 (2006).

[21] B. Lorentz, Y.-Q. Wang, and C.-W. Chu, Phys. Rev. B 76, 104405 (2007).

[22] M. E. Fisher, and W. Selke, Phys. Rev. Lett. 44, 1502 (1980).

[23] S. Rayaprol *et al.*, Sol. Stat. Comm. **128**, 79 (2003).

- [24] V. G. Zubkov et al., J. of Sol. Stat. Chem. 160, 293 (2001).
- [25] A. Maignan et al., Eur. Phys. J. B, 15, 657 (2000).
- [26] J. Rodriguez-Carvajal, Physica B 192, 55 (1993).
- [27] J. A. Mydosh, *Spin Glasses. An Experimental Introduction*. (Taylor & Francis, London, 1993).

Chapter V

Giant Magnetic Coercivity change induced by co-operative freezing in Ca₃Co₂O₆

1. Introduction

Materials with large coercivity are widely used in our daily lives as a magnetic recording, sensors, motors and even medical applications. It is reported that the saturated magnetization is removed by the rotation of spin direction and the growth of reverse domains or nucleation with the energy of the external field. To achieve large coercivity, these mechanisms must be impeded. The rotation of magnetization is controlled by crystal anisotropy. The growth of reverse domains can be encumbered with defects as pinning centers [1]. By this reason, the large coercivity value is usually achieved from polycrystalline samples and alloys [2]. It is interesting to note that the large coercivity value is observed in $Ca_3Co_2O_6$ single crystal. Recently, many studies in $Ca_3Co_2O_6$ have been performed due to its peculiar magnetic properties. These properties are closely related with the geometrical frustration and low dimensionality. The rhombohedral Ca₃Co₂O₆ structure consists of chains, which is formed by the CoO₆ octahedral and the trigonal prism alternatively. Ferromagnetically ordered Co chains, which spin within one dimension chain, are separated by nonmagnetic Ca ions. These Co spins are aligned in ab plane with geometrically frustrated honey comb structure (six triangular lattices). The Ca₃Co₂O₆ has complex magnetic ordering states. Ferromagnetic short range spin ordering in intra chain starts from ~200 K, while 2-D short range antiferromagnetic ordering in inter chain starts from ~100 K. As temperature reaches 24 K, Partially Disordered Antiferromagnetism (PDA) state appears [3]. And Magnetic Quantum Tunneling (MQT) and Hysteresis are reported at low temperature [4,5]. In here, we will focus on the relation between spin freezing-like features and coercivity change.

2. Experimental Method

In order to examine the coercivity change and spin freezing like features of $Ca_3Co_2O_6$ single crystal, the magnetic properties like D.C. susceptibility ($\chi_{dc} = dM/dH$) and magnetization (M(H)) were studied at various temperatures as well as a.c. susceptibility and specific heat. These measurements were performed on Quantum Design MPMS and PPMS system.

We studied a $Ca_3Co_2O_6$ single crystal sample grown by the flux method using polycrystalline $Ca_3Co_2O_6$ with K_2CO_3 and KCl [4:1] as the flux mixture [3]. The $Ca_3Co_2O_6$ polycrystalline sample was prepared using the solid reaction method with several intermediate grinding and sintering. The mixture of polycrystalline $Ca_3Co_2O_6$, K_2CO_3 and KCl was heated at 1193 K for 10 hours in air, and then cooled down to 1073 K with 1 K/h cooling rate. Needle shape samples were successfully obtained. The phase stoichiometry of our samples was confirmed by powder X-ray diffraction measurement.

3. Results and Discussion

The zero field cooling (ZFC) and field cooling (FC) susceptibility ($\chi(T)$) curves in an applied field (parallel and perpendicular to c-direction) of 2 kOe are shown in Fig. IV. 1(a). With decreasing temperature from the paramagnetic region, the sharp slope change was observed at 24 K (T_c), which corresponds to long range ferromagnetic ordering in intra-chain [3]. As the temperature fell further, irreversibility features between ZFC and FC susceptibility curves were observed at 12 K (T_{sp}).

The irreversibility feature is a common signature of a spin freezing like system. Another spin freezing like feature is reported below 5 K (T_{sf}) [4], which corresponds to

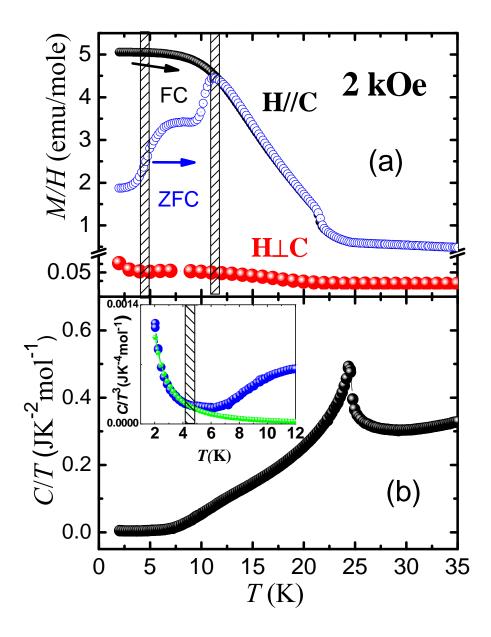


FIG. IV. 1. (a) Temperature dependence of the magnetic susceptibility, the magnetic field (2 kOe) was applied along c direction (blue color and black color as a ZFC and FC, respectively) and perpendicular c direction (red), two shading regions indicate the approximate region in which the spin freezing like features appear. (b) C/T versus temperature specific heat data, while the inset picture shows the C/T^3 versus temperature.

the highest slope in our ZFC curve. The strong crystal anisotropy is also shown in FIG. IV. 1(a). The easy axis is along the $(Co_2O_6)\infty$ chain direction. The susceptibility of an easy axis is two orders larger than that of hard axes. The specific heat clearly indicates the T_c at 24 K, as shown by the peak in FIG. IV. 1(b), *C/T* versus *T* graph. The *C/T* (*T*) curve shows a little hump at 12 K and also a linear contribution γT below ~ 6 K in agreement with other papers [6]. The low temperature specific heat data will be discussed later in this paper.

To analyze spin freezing like (irreversibility) features at 12 K and 5 K, respectively, a real and an imaginary part of a.c. susceptibility measurement was performed on this sample. The χ' of the frequency dependent magnetic susceptibility is shown in FIG. IV. 2(a) and (b), respectively. In the case of spin freezing like feature at 12 K, as the frequency changes from 10 Hz to 10 KHz, the χ ' and χ '' data shows a clear change in T_{fmax} (temperature|_{highest χ'}). The log (f(Hz)) versus T_f^{-1} curve is shown in the inset FIG. IV. 2(a). The Ca₃Co₂O₆ shows physically reasonable Arrhenius behavior, which is defined in terms of $f = f_0 \exp(-E_a/K_BT_f)$, values with a $f_0 = 1$ GHz (f value for infinite temperature) and an activation energy of $E_a \sim 240$ K. The quantified frequency variation value, which is defined in terms of $P = \Delta T_{fmax} / T_{fmax} \Delta \log(f_{AC})$, was approximately 0.16. This large p value indicates that the 12 K spin glass like feature comes from superparamagnet phenomena [7,8]. It is hard to find a distinct peak and frequency dependence for a spin freezing like feature at 5 K despite a broad little hump in the χ ' data of the corresponding 10 Hz case. Many researches claim to have observed a spin freezing state below the 5 K state with their M(T), specific heat and various waiting time M(H) data [6, 9, 10], even though the transition temperature is not well defined

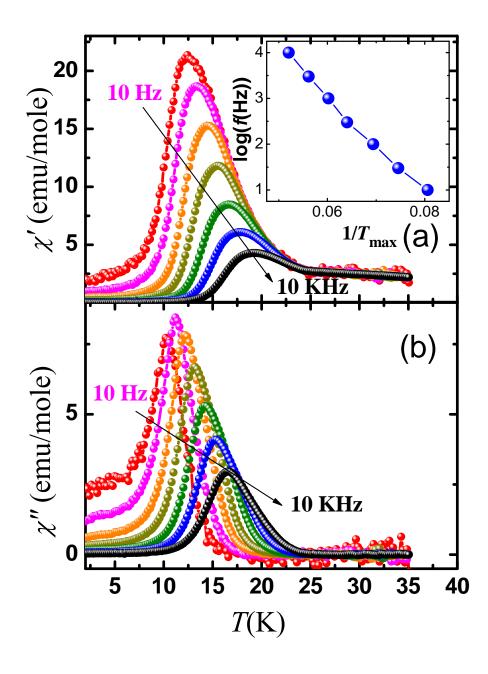


FIG. IV. 2. (a) Real part of the a.c. susceptibility with function of temperature at different frequencies (10, 30, 100, 300, 1 K, 3 K, and 10 KHz). The inset picture shows the measurement frequency (log scale) versus the inverse of the freezing temperature. (b) Imaginary part of the a.c. susceptibility in terms of temperature.

(differs from 4 K to 8 K). Our M(T) data shows the highest slope in ZFC curve at 5 K. The specific heat plot shows constant value below ~6 K, as mentioned before. This constant region in C/T versus T is related with linear behavior in C versus T. At low temperature, the linear behavior of the specific heat value is argued as a starting point for the spin glasses [6, 8]. To clearly observe the low temperature specific heat data, the C/T^3 versus T graph is plotted as an inset of FIG. IV. 1(b). The a/T^2 (a is a constant) curve fit well with C/T^3 versus T curve until 5 K from 2 K, which is corresponding with the linear region in C versus T. This region is mentioned as a starting point of spin freezing state.

The M (H) data shows a plateau at 1/3 of the saturated magnetization value (1/3 M_s) from the T_c to the T_{sf}. Below T_{sf}, the number of steps increases with decreasing temperature as shown in FIG. IV. 3(a). As shown in FIG. IV. 3(b), there are 5 steps for 2 K. The M (H), dM/dH, and χ " at different frequencies versus H consistently show constant field spacing of 1.2 T among steps. These M (H) steps at 2 K are defined in terms of QTM [4,5]. The 1/3 M_s plateau also comes from the peculiar magnetic properties of Ca₃Co₂O₆. One incoherent chain is induced by the triangular geometrical frustration, while other two chains are antiferromagnetically coupled. As the external field increases, the 1/3 incoherent chain aligned along the external field. By this reasoning, the 1/3 M_s plateau state is expressed in terms of a PDA or 'dynamic ferromagnetic' state [3,11].

The inset of FIG. IV. 3(a) shows the normalized M(H) curves at various temperatures. The data shows the slope change at 1/3 M_s, with decreasing temperature. The slope decreases from 24k to 12 K and then increases again until 5 K. As the temperature fells down from 5 K, sharp slope increasing is observed. The applied field (H_{1/3Ms}) corresponds to 1/3 M_s versus temperature is plotted in FIG. IV. 5(b). From T_c to

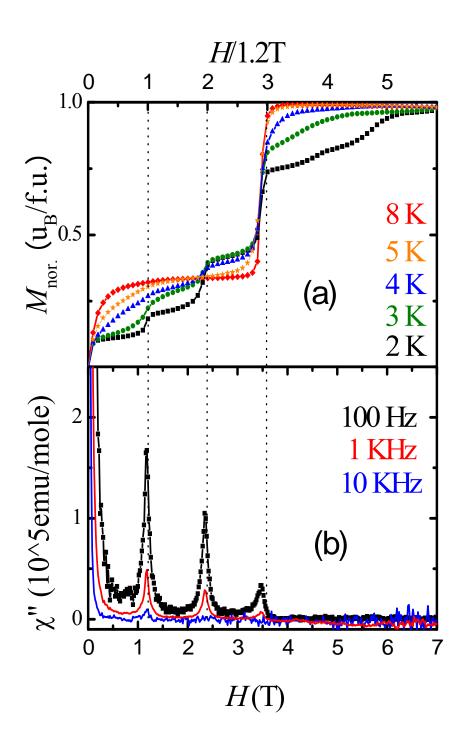


FIG. IV. 3. (a) Normalized magnetization versus applied magnetic field at different temperature. (b) Imaginary part of a.c. susceptibility with function of applied magnetic field at various frequencies.

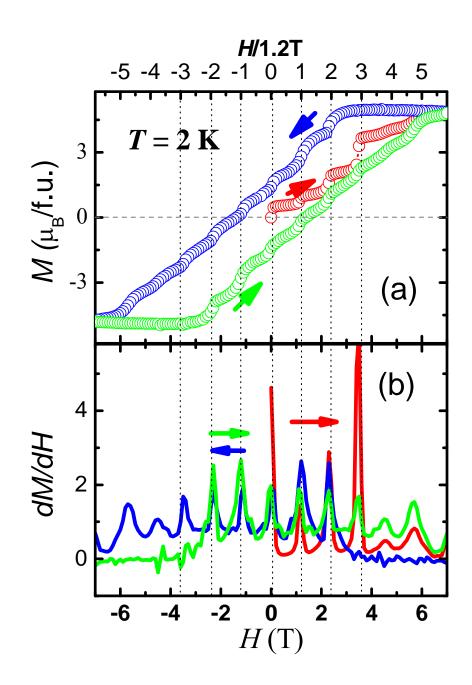


FIG. IV. 4. (a) Hysteresis loop at T = 2 K. (b) dM/dH versus applied magnetic field. Dashed lines in figure shows n multiply H/1.2 Tesla (where n is integer).

about 5 K, whole M(H) curves meet at 2 Tesla, which is corresponding to H value for 1/3 $M_{s.}$ This point merging feature of $H_{1/3Ms}$ is consistent with Monte Carlo simulation result [12], even though, the $H_{1/3Ms}$ merged at 1.8 Tesla in simulation case. As mentioned in the introduction of this paper, $Ca_3Co_2O_6$ has a honey comb structure in a-b plane. As the temperature crosses the T_c, the six chains, which surround undetermined spin, start to align up and down alternately. Then surrounding spins are fully aligned at T_{sp.} During this alignment process, the magnetization of this system more easily reaches the $1/3 M_s$ value and the plateaus become broader with decreasing temperature. As the temperature is lowered further from the T_{sp} to the T_{sf} , the slope increases and the plateau decreases again, because the system undergoes the freezing. As passing the $T_{\rm sf}$ (below 5 K), the slope sharply increases and H_{1/3Ms} value also increases up to 2.32 Tesla at 2 K. It means that we need keep increasing the external field to reach the $H_{1/3Ms}$ value, while decreasing temperature. This observation indicates the co-operative interactions among clusters or nano-particles exist in this spin freezing state and the co-operative interactions make it harder and harder to reach the $H_{1/3Ms}$ value, as temperature decreases.

We now turn to the coercivity data. As shown in FIG. IV. 5(c), no coercivity is observed until 12 K, while negligible coercivity is observed from 12 K to 5 K. From about 5 K and below, the coercivity increases dramatically up to 1.38 Tesla at 2 K. The region showing the giant change in the coercivity is consistent with the temperature region showing an increasing in the applied field for the $H_{1/3Ms}$ value. This region also matched well with the large slope change region as shown in FIG. IV. 6. This analysis indicates that the co-operative spin freezing plays an important role in the giant coercivity change in Ca₃Co₂O₆. The magnitudes of multiple energy barriers increased below spin

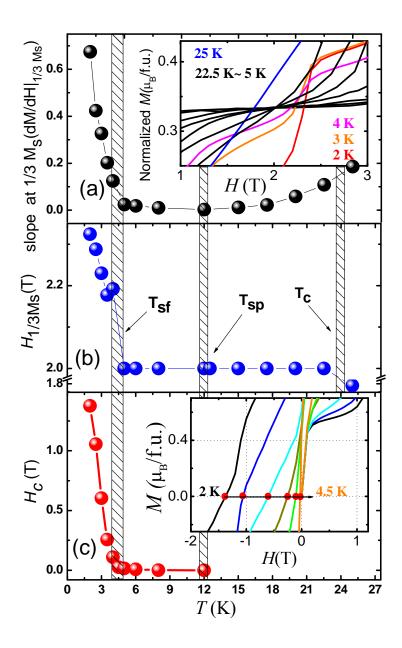


FIG. IV. 5. (a) Slope at $1/3 \text{ M}_{s} (dM/dH|_{1/3Ms})$ versus applied magnetic field, while the inset plot shows the magnetization with function of applied magnetic field at various temperatures. (b) The applied field (H_{1/3Ms}) corresponds to $1/3M_{s}$ value versus temperature. T_c, T_{sp}, and T_{sf} indicate the long range ordering, superparamagnet, and spin freezing temperature, respectively. (c) Coercivity versus temperature. Inset, magnetization versus applied field at different temperature. Red spots indicate the coercivity value.

freezing temperature in the co-operative spin glasses [8]. The increased energy barriers encourage that the co-operative spin state is less affected by external perturbations. There is an observation of coercivity increasing below freezing temperature in a co-operative spin glasses. But the coercivity does not exceed 200 Oe at their lowest temperature (1.2 K) [14], while the coercivity increased up to 1.38 Tesla at 2 K in our case. At this point, we note that the low dimensionality of Ca₃Co₂O₆ plays a role in large coercivity with giant coercivity change.

4. Conclusions

In conclusion, the geometrically frustrated and disordered one dimensional chain, Ca₃Co₂O₆, system is analyzed. Spin freezing like features were observed in M(T) and specific heat data at 12 K and below 5 K respectively. The spin freezing like state for 12 K is concluded to be a superparamagnet state, which has no co-operative spin interactions among clusters or nano-particles. That for below 5 K is analyzed as a co-operative magnetic freezing state. With decreasing temperature in the co-operative magnetic freezing state, the coercivity dramatically increases from zero to 1.38 Tesla. Meanwhile the slope values of M(H) curves at $1/3M_s$ also sharply increases with increasing in applied magnetic field value at $1/3M_s$. These observations mean that the large coercivity with giant magnetic coercivity change in Ca₃Co₂O₆ is induced by the co-operative spin freezing with a low-dimensionality. This result is clearly distinct from previously known mechanism for large coercivity. Because the observation of coercivity is limited in spin freezing state and also the amount of defects in our single crystal sample is negligible. We propose the co-operative spin freezing with a low-dimensionality as a new mechanism for large coercivity. We hope that this new and promising mechanism will help to spur enhancement of the coercivity and also theoretical efforts in this field.

5. REFERENCES

[1] J. D. Livingston., J. Appl. Phys. 52, 2544-2548 (1981).

[2] M. F. de Campos et al., J. Appl. Phys. 84, 368-373 (1998).

[3] A. Maignan, C. Michel, A. C. Masset, C. Martin, and B. Raveau., Eur. Phys. J. B. 15, 657-663 (2000).

[4] V. hardy, D. Flahaut, M. R. Lees, and O. A. Petrenko., Phys. Rev. B. 70, 214439 (2004).

[5] A. Maignan et al., J. mater. Chem. 14, 1231-1234 (2004).

[6] V. Hardy, S. Lambert, M. R. Lees, and D. McK. Paul, Phys. Rev. B. 68, 014424 (2003).

[7] J. A. Mydosh. Spin Glasses, An Experimental Introduction. (Taylor & Francis, London, 1993)

[8] J. Snyder, J.Slusky, R. J. Cava, and P. Schiffer, Nature (London) 413, 48-51 (2001).

[9] H. kageyama et al., J. Phys. Soc. Jpn. 66, 1607-1610 (1997).

[10] V. Hardy, et al., Phys. Rev. B. 70, 064424 (2004).

[11] S. Takeshita et al., J. Phys. Soc. Jpn. 75, 03712 (2006).

[12] X. Yao, S. Dong, H. Yi, and J. Liu, Phys. Rev. B. 74, 134421 (2006).

[13] S. T. Bramwell, and M. P. Gingras, Science 294, 1495-1501 (2001).

[14] S. Senoussi, S. Hadjoudy, and R. Fourmeaux, Phys. Rev. Lett. **61**, 1013-1016 (1988).

Chapter VI

Conclusions

In this chapter, I summarized key points of this thesis and discuss the future study in this field. In chapter I, we have discussed the definition, applications, and classification of fascinating usage of transition metal oxide materials.

In chapter II, we report cryogenic-temperature phase-change random access memory (cryoP-RAM) effect in TMO material. Cryogenic-temperature electronics technologies with, e.g., many types of quantum computers, Superconducting Rapid Single Flux Quantum (RSFQ) devices, and cryogenic detectors are a practical promise for continuing demand for high performance electronics. One of the critical bottle necks for cryo-electronics is low-temperature memories. By utilizing the unique hysteretic behavior of perovskite (La,Pr,Ca)MnO₃ in the variation of temperature and applied electric fields, we have discovered 1) low-temperature phases with metallic and insulating resistance values (different by $>10^5$) can be repeatedly switched by applying various voltage pulses, 2) the resistance value of each phase is highly repeatable through cycling and also stable with time, and 3) intermediate phases with intermediate resistance values can be also repeatedly stabilized. These behaviors can enable cryoP-RAM applications, compatible with, e.g., the RSFQ technology.

In chapter III, we report the ferroelectric photovoltaic (FPV) effect in BiFeO₃ and significant rectification effects exist in BiFeO₃, and the direction of the rectification and photovoltaic current is reversely switchable by large external voltages. The forward bias direction is along the ferroelectric polarization direction and short circuit currents after positive poling is $-1.26 \,\mu$ A/cm², whereas *I*_{sc} after negative poling is $+0.95 \,\mu$ A/cm² with a good retention and high stability over cycling. We confirmed that the polarization clearly plays an essential role on the rectification and photovoltaic effects by PFM and poling-

voltage dependence of rectification direction switching measurement. As a possible scenario, the switchable Schottky-to-Ohmic mechanism was proposed. To verify a existence of the bulk effect, the four probe measurement was performed in BFO sample and rectification effect observed clearly. Further study of these effects, such as experiments involving different ferroelectric materials and/or controlled doping levels will be necessary to unveil the true origin. By engineering the band gap, carrier concentration, and device configurations, this fascinating switchable diode and photovoltaic effects need to be further exploited for novel technologies such as fast readout of ferroelectric state, ferroelectric solar cells, or ferroelectric sensors.

In chapter IV, we report discovery of collinear-magnetism-driven ferroelectricity in the Ising chain magnet $Ca_3Co_{2-x}Mn_xO_6$ (x \approx 0.96). Neutron diffraction shows that Co^{2+} and Mn^{4+} ions alternating along the chains exhibit an up-up-down-down ($\uparrow\uparrow\downarrow\downarrow\downarrow$) magnetic order. The ferroelectricity results from the inversion symmetry breaking in the ($\uparrow\uparrow\downarrow\downarrow\downarrow$) spin chain with an alternating charge order. Unlike in spiral magnetoelectrics where antisymmetric exchange coupling is active, the symmetry breaking in $Ca_3(Co,Mn)_2O_6$ occurs through exchange striction associated with symmetric superexchange.

In chapter V, we discussed the high coercivity in $Ca_3Co_2O_6$. The large coercivity – large external field which is required to fully remove the saturated magnetization in material - has been extensively researched with its attractive character in application. The large coercivity is usually realized when crystal anisotropy and pinning center by defects are satisfied. Herein, we report new mechanism for increasing coercivity. The large coercivity is observed in a $Ca_3Co_2O_6$ single crystal, which has a one dimensional chain structure. The giant change in coercivity is observed from zero to 1.38 Tesla with decreasing temperature. This coercivity change is performed in a co-operative spin freezing state. We propose the co-operative spin freezing with a low dimensionality as a new and promising mechanism to enhance the coercivity.

There are still many things we have to overcome to realize a genuine application to real life. The first thing is that the temperature range in which the most interesting effects can be observed is still too low to be useful in practice specially in multiferroic and high coercivity. The second thing will be that it usually requires pretty high electric fields to manifest a high on-off switch in existing cryo-PRAM using LPCMO and photocurrent direction switching in BiFeO₃. Another obstacle is that the exact mechanism for switchable photovoltaic effect is very subtle to extract from the data. In the experimental point of view, although the effect of oxygen deficiency migration and polarization is pretty well known, the understanding of the exact mechanism origins from whether combined two effects or existence of dominant effect is still immature. More research in interface between electrode and bulk can surely bring about our better understanding and help to develop new photovoltaic materials.

Curriculum Viate

Hee Taek Yi

EDUCATION

2004-2010	Ph.D. Electrical and Computer Engineering Rutgers, The State University of New Jersey, New Brunswick, NJ
2002-2004	M.S. Electrical and Computer Engineering Rutgers, The State University of New Jersey, New Brunswick, NJ
1998-2000	M.S. Electrophysics Kwangwoon University, Seoul, South Korea
1992-1998	B.S. Physics Kwangwoon University, Seoul, South Korea

POSITIONS HELD

2006-2010	Graduate Research Assistant
	Rutgers University Physics department

1998-2000 Student Researcher Korea Institute of Science and Technology (KIST), Seoul, Korea

PUBLICATIONS

- Insulating Interlocked Ferroelectric and Structural Antiphase Domain Walls in Multiferroic YMnO₃.
 T. Choi, Y. Horibe, <u>H. T. Yi</u>, Y. J. Choi, W. Wu, & S-W. Cheong, *Nature Materials* 9, 253 (2010)
- Spin-state crossover in multiferroic Ca₃Co_{2-x}MnxO₆.
 R. Flint, <u>H. T. Yi</u>, P. Chandra, S.-W.Cheong & V. Kiryukhin, *Phys. Rev. B* 81, 092402 (2010)
- Reversible colossal resistance switching in (La,Pr,Ca)MnO₃. <u>H. T. Yi</u>, T. Choi & Sang-Wook Cheong, *Appl. Phys. Lett.* 95, 063509 (2009)
- Spin freezing and dynamics in Ca₃Co_{2-x}MnxO₆ (x~0.95) investigated with implanted muons: Disorder in the anisotropic next-nearest-neighbor Ising model. T. Lancaster, S. J. Blundell, P. J. Baker, H. J. Lewtas, W. Hayes, F. L. Pratt, <u>H. T. Yi</u>, & S.-W.Cheong, *Phys. Rev. B* 80, 020409(R) (2009)

- Order by Static Disorder in the Ising Chain Magnet Ca₃Co_{2-x}Mn_xO₆.
 V. Kiryukhin, Seongsu Lee, W. Ratcliff II, Q. Huang, <u>H. T. Yi</u>, Y. J. Choi, & S-W. Cheong, *Phys. Rev. Lett.* **102**, 187202 (2009)
- 3:1 magnetization plateau and suppression of ferroelectric polarization in an Ising chain multiferroic
 Y. J. Jo, S. Lee, E. S. Choi, <u>H. T. Yi</u>, W. Ratcliff II, Y. J. Choi, V. Kiryukhin, S. W. Cheong, & L. Balicas, *Phys. Rev. B* 79, 012407(2009)
- Formation of pancakelike ising domains and giant magnetic coercivity in ferrimagnetic LuFe₂O₄.
 WeidaWu, V. Kiryukhin, H.-J. Noh, K.-T. Ko, J.-H. Park, W. Ratcliff II, P. A. Sharma, N. Harrison, Y. J. Choi, Y. Horibe, S. Lee, S. Park, <u>H. T. Yi</u>, C. L. Zhang, & S.-W. Cheong, *Phys. Rev. Lett.* **101**, 137203 (2008)
- Multiferroicity in the square-lattice antiferromagnet of Ba₂CoGe₂O₇. <u>H. T. Yi,</u> Y. J. Choi, S. Lee & Sang-Wook Cheong, *Appl. Phys. Lett.* 92, 212904 (2008)
- Ferroelectricity in an Ising chain magnet.
 Y. J. Choi, H. T. Yi, S. Lee, Q. Huang, V. Kiryukhin, & S.-W. Cheong, *Phys. Rev. Lett.* 100, 047601 (2008)